Featured in Physics

Emergent chirality in active solid rotation of pancreas spheres

Tzer Han Tan,[1,2,3] Aboutaleb Amiri,[1] Irene Seijo-Barandiaran,[2] Michael F. Staddon,[1,2,3] Anne Materne,[1] Sandra Tomas,[2,4] Charlie Duclut,[1,5,*] Marko Popović,[1,3,6,†] Anne Grapin-Botton,[2,3,6,‡] and Frank Jülicher[1,3,6,§]

[1]*Max Planck Institute for the Physics of Complex Systems, Dresden, Germany*
[2]*Max Planck Institute of Molecular Cell Biology and Genetics, Dresden, Germany*
[3]*Center for Systems Biology Dresden, Dresden, Germany*
[4]*Center for Molecular and Cellular Bioengineering, Technische Universität Dresden, Dresden, Germany*
[5]*Université Paris Cité, Laboratoire Matière et Systèmes Complexes (MSC), UMR 7057 CNRS, Paris, France*
[6]*Cluster of Excellence Physics of Life, Technische Universität Dresden, Dresden, Germany*

(Received 14 January 2024; accepted 8 July 2024; published 8 August 2024)

Collective cell dynamics play a crucial role in many developmental and physiological contexts. While two-dimensional (2D) cell migration has been widely studied, how three-dimensional (3D) geometry and topology interplay with collective cell behavior to determine dynamics and functions remains an open question. In this work, we elucidate the biophysical mechanism underlying rotation in spherical tissues, a phenomenon widely reported both *in vivo* and *in vitro*. Using murine pancreas-derived organoids as a model system, we find that epithelial spheres exhibit persistent rotation, rotational axis drift, and rotation arrest. Using a 3D vertex model, we demonstrate how the combined action of traction force and polarity alignment can account for these distinct rotational dynamics near a solid to flow transition. Furthermore, our analysis shows that the spherical tissue rotates as an active solid occasionally switching to a flowing state and exhibits spontaneous chiral symmetry breaking. Using a continuum model, we demonstrate how the topological defects in the polarity field underlie this symmetry breaking process, which is revealed by asymmetries in the cell elongation pattern. For cell elongation to reveal the chiral asymmetry, shear flow is required in addition to the solid body rotation. Altogether, our work reveals a robust chiral symmetry breaking mechanism with potential implications for left-right symmetry breaking processes in morphogenetic events.

DOI: 10.1103/PRXLife.2.033006

I. INTRODUCTION

Collective cell migration is an important phenomenon in many biological systems [1], ranging from bacterial colonies [2,3] to morphogenesis [4] and wound healing in multicellular organisms [5]. Through the interplay between directed motion, neighbor alignment, and mechanical interactions, cell collectives exhibit emergent structures and dynamics that are crucial for their function. These include topological defects in two-dimensional (2D) [6,7] and 3D [8,9] tissues during morphogenesis, jamming transition during vertebrate body axis elongation [10], and chiral tissue flows during gastrulation [11]. Recent work in synthetic active matter shows that curved surfaces and topological constraints can modulate the collective dynamics in active matter systems, resulting in shape changing vesicles [12], curvature-dependent defect unbinding [13], and topological sound [14]. This raises the question of how geometry and topology govern the emergence of collective patterns of cell migration from cellular properties and cell interactions.

In recent years, several studies have explored how geometrical confinement through micropatterns can govern the coordinated movements of cells, such as the persistent rotation of Madin-Darby canine kidney (MDCK) cells on fibronectin coated circular micropatterns [15] and the chirally asymmetric collective movement of mouse myoblast cells on ring-shaped micropatterns [16]. Computational work using Potts models has revealed how circular patterns can drive swirl-like collective movements when cell density is increased [17] and a chemomechanical vertex-model demonstrates how distinct migration modes can emerge through through the interplay of internal cellular activities and exterminal geometrical constraints [18].

Extending beyond flat geometries, rotation behaviors have been observed in three-dimensional cell colonies. The prominent phenomenon of tissue rotation in spherical geometry has been reported both *in vitro*, in the case of MDCK spheres [19–21], epithelial cell colonies [22], and cancer spheroids [23], and *in vivo*, as in *Drosophila melanogaster* egg chamber rotation [24]. Rotations were also recently described in MDCK cells in tubular geometry [25,26] and in organoid

*Present address: Laboratoire Physico-Chimie Curie, CNRS UMR168, Institut Curie, Université PSL, Sorbonne Université, 75005, Paris, France.
†Contact author: mpopovic@pks.mpg.de
‡Contact author: botton@mpi-cbg.de
§Contact author: julicher@pks.mpg.de

systems derived from primary cells or cell lines from the mammary gland [27–30], indicating that tissue rotation is an intrinsic process of many 3D multicellular structures. Yet, the biophysical mechanisms underlying tissue rotational dynamics and how different rotational modes can be biologically controlled remain open questions.

In this work, we study the collective motion of cells in spherical pancreas organoids (henceforth called pancreas spheres), which exhibit rotational and arrested states. We find that during sphere rotation, patterns of cell motion and cell shape reveal a broken chiral symmetry of the sphere. We use vertex model and continuum theory to identify the underlying causes of this symmetry breaking. We find that stochastic switching between rotating and arrested states can be explained as the result of a solid to fluid transition driven by active traction forces. We propose that chiral symmetry of spheres is broken by the underlying pattern of cell traction forces. This chirality is revealed in cell shape patterns during rotational motion near the solid to fluid transition.

II. DISTINCT ROTATIONAL DYNAMICS IN PANCREAS SPHERES

Here, we use pancreas spheres, derived from mouse pancreas progenitor cells [31] (see Appendix A), as a model to investigate the collective cell motion in tissue rotation and their broken symmetries. These pancreas spheres are single-layer epithelia with apico-basal polarity. The apical side faces the fluid-filled lumen while the basal side faces outwards towards the Matrigel (which acts like an extracellular matrix) [31] Fig. 1(a). Live imaging experiments show that pancreas spheres derived from E13.5 mice exhibit a range of dynamics, some rotating [Supplemental Material (SM) Video 1 [32]], some static (SM Video 2), some stopping (SM Video 3), and some changing axis (SM Video 4).

To quantitatively characterize the complex rotational dynamics, we develop a computational pipeline to segment the spheres' apical surface and visualize their fluorescence intensity by a Mercator projection [Figs. 1(b) and 1(c), Appendix B 1]. By performing particle image velocimetry (PIV) analysis, we find that the resultant time-lapsed projection shows long-range correlated tissue flow, with localized vortical motion that corresponds to the two poles of tissue rotation (Fig. 7; SM Video 5). This confirms that collective cell migration underlies the rotational motion of pancreas spheres.

To determine the angular velocity and the rotation axis, we reconstructed the full three-dimensional (3D) tissue flow field on the sphere [Fig. 1(d) and Appendix B 3] and computed its angular momentum (see Appendix B 4). We find that the azimuthal velocity with respect to the instantaneous rotation axis follows a sine profile [Fig. 1(e)], suggesting that the pancreas spheres act as a solid body when rotating.

The dynamics of the pancreas sphere observed on shorter timescales up to 4 h can be classified as either rotating [Fig. 1(f),(i) and Fig. 8] or nonrotating [Fig. 1(f),(ii) and Fig. 8]. During persistent rotation, the angular speed remains roughly constant and the orientation of rotation axis remains stable. In contrast, when there is no rotation, the sphere is characterized by a small angular speed and large jumps in rotation axis orientation. Observing the dynamics of pancreas spheres on longer timescales up to 15 h allowed us to capture transitions between the rotating and nonrotating states [Fig. 1(g),(i) and Fig. 8]. During a transition, the angular velocity slows down and the rotation axis becomes unstable, leading to a marked increase in axis angle change [Fig. 1(g),(i)]. Furthermore, we have observed persistently rotating spheres that occasionally change their axis of rotation [Fig. 1(g),(ii) and Fig. 8]. This is characterized by a slow meandering in the orientation of rotation axis, coinciding with periods of lower angular velocity and a higher rate of axis angle change. The diverse dynamics described above could be seen simultaneously in the same culture (Fig. 9). We tested whether these changes in sphere dynamics could be due to variability of the material properties of the surrounding matrix. We found that the material properties remained essentially unchanged over the course of experiments (Appendix B 7 and Fig. 10), consistent with previous report [33]. These observations raise the question of whether the rich dynamic behavior of pancreas spheres can be understood as an emergent property of cell mechanics, force generation, and cell interactions.

III. SOLID AND FLOWING REGIMES OF AN ACTIVE VERTEX MODEL

To identify the physical principles underlying the observed pancreas sphere dynamics, we developed a vertex model of pancreas spheres in 3D spherical geometry. Vertex models have been used to study the mechanical aspects of epithelial morphogenesis that regulate their packing geometry [34], motility-driven rigidity transition [35], and developing tissues as amorphous solids that exhibit yielding transition under shear [36]. Due to the active nature of our system, we included two necessary ingredients: (i) active traction force, which allows the cells to move with respect to the ECM; and (ii) cell polarity, which determines the direction of the active traction force.

Specifically, we extend the model in [34] to a spherical geometry and define the forces stemming from the mechanical properties of individual cells and the interaction between them based on the work function

$$W = \sum_{\alpha \in \text{cells}} \frac{1}{2} K^{\alpha} \left(A^{\alpha} - A_0^{\alpha}\right)^2 + \sum_{\alpha \in \text{cells}} \frac{1}{2} \Lambda^{\alpha} L^{\alpha}. \tag{1}$$

This model captures the cell shapes on the sphere surface as polygons. The first term accounts for cell area elasticity, with A_0^{α} being the preferred cell area and K^{α} the area stiffness. The second term accounts for cell bond tension, where Λ^{α} is the bond tension magnitude, and L^{α} denotes the cell perimeter [34,37]. Here, we consider for simplicity the case in which the mechanical parameters are uniform in the tissue and equal for all cells: $K^{\alpha} = K$, $A_0^{\alpha} = A_0$, and $\Lambda^{\alpha} = \Lambda$. At each vertex m located at position $\boldsymbol{X}_m$, the vertex force $-\partial W/\partial \boldsymbol{X}_m$ is balanced by traction force $F\langle \boldsymbol{p} \rangle_m - \xi \boldsymbol{v}_m$:

$$\xi \boldsymbol{v}_m = F\langle \boldsymbol{p} \rangle_m - \frac{\partial W}{\partial \boldsymbol{X}_m} + f_m^n \hat{\boldsymbol{n}}_m, \tag{2}$$

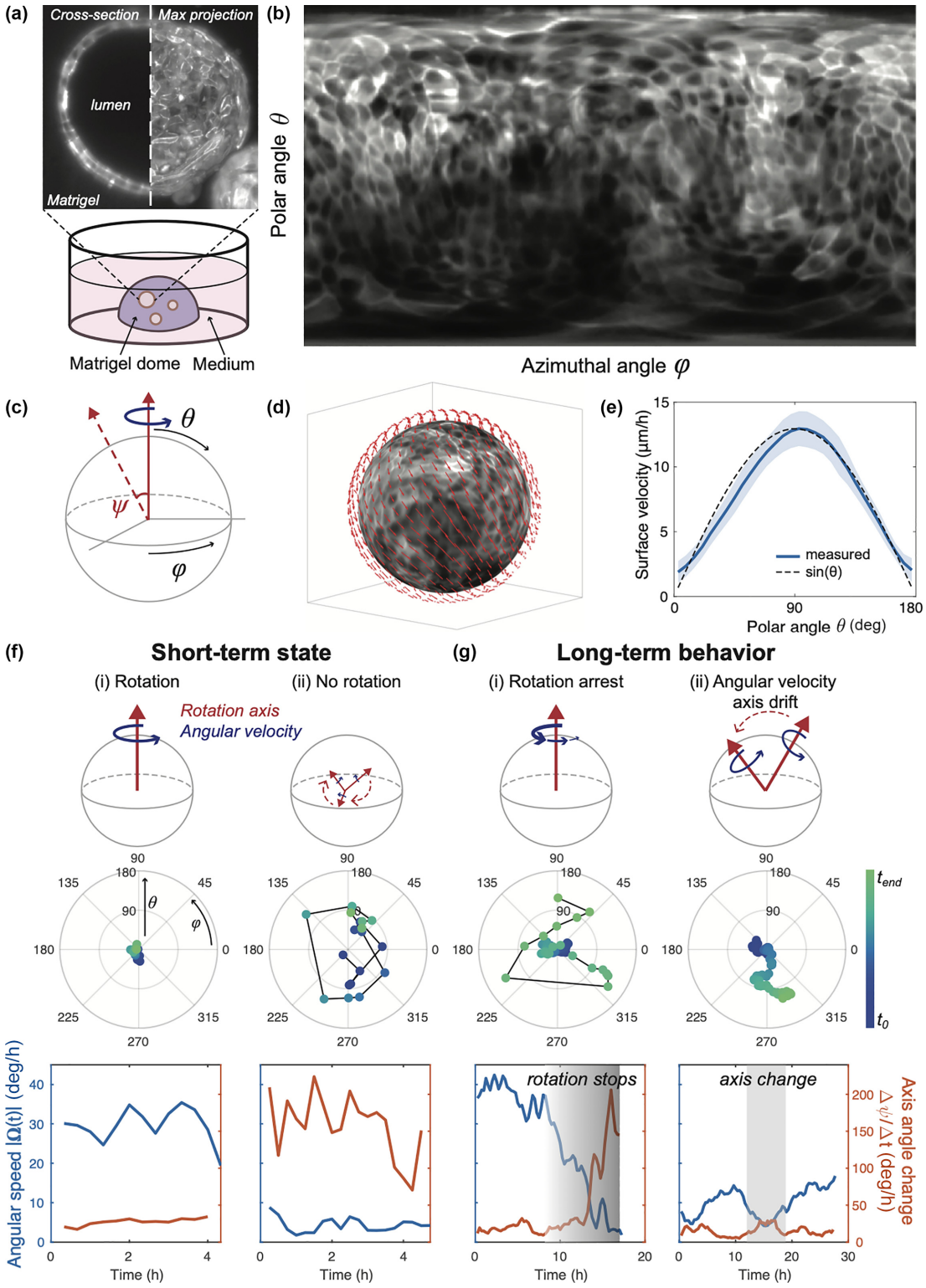

FIG. 1. Distinct rotational dynamics in pancreas spheres. (a) Experimental setup: pancreas progenitor cells form single layer epithelial spheres (gray: Myh14 signal) when cultured in Matrigel. (b) Mercator projection of the apical surface of a pancreas sphere (gray: Myh14 signal). (c) Schematic defining the angular conventions: ϕ denotes azimuthal angle, θ is the polar angle, and ψ is the angular change of rotation axis. (d) Surface velocity of a rotating sphere (gray: Myh14 signal) as measured by particle image velocimetry (PIV, red vectors). (e) Surface velocity of a rotating sphere as a function of polar angle θ. (f), (g) Rotational dynamics that pancreas spheres exhibit in the short (f) and long (g) term. The first row shows a schematic for the type of rotational dynamics. The second row shows the angular position of the rotation axis as a function of time in the (θ, ϕ) polar plot. The third row shows the magnitude of the angular velocity and the rotational axis angular change. We show a representative case for each type of dynamics here. Additional data are included in Figs. 8 and Fig. 9. Error bars in (e) are the standard deviation of temporally and azimuthally averaged PIV velocities ($N \approx 1000$ per time point over 30 time points).

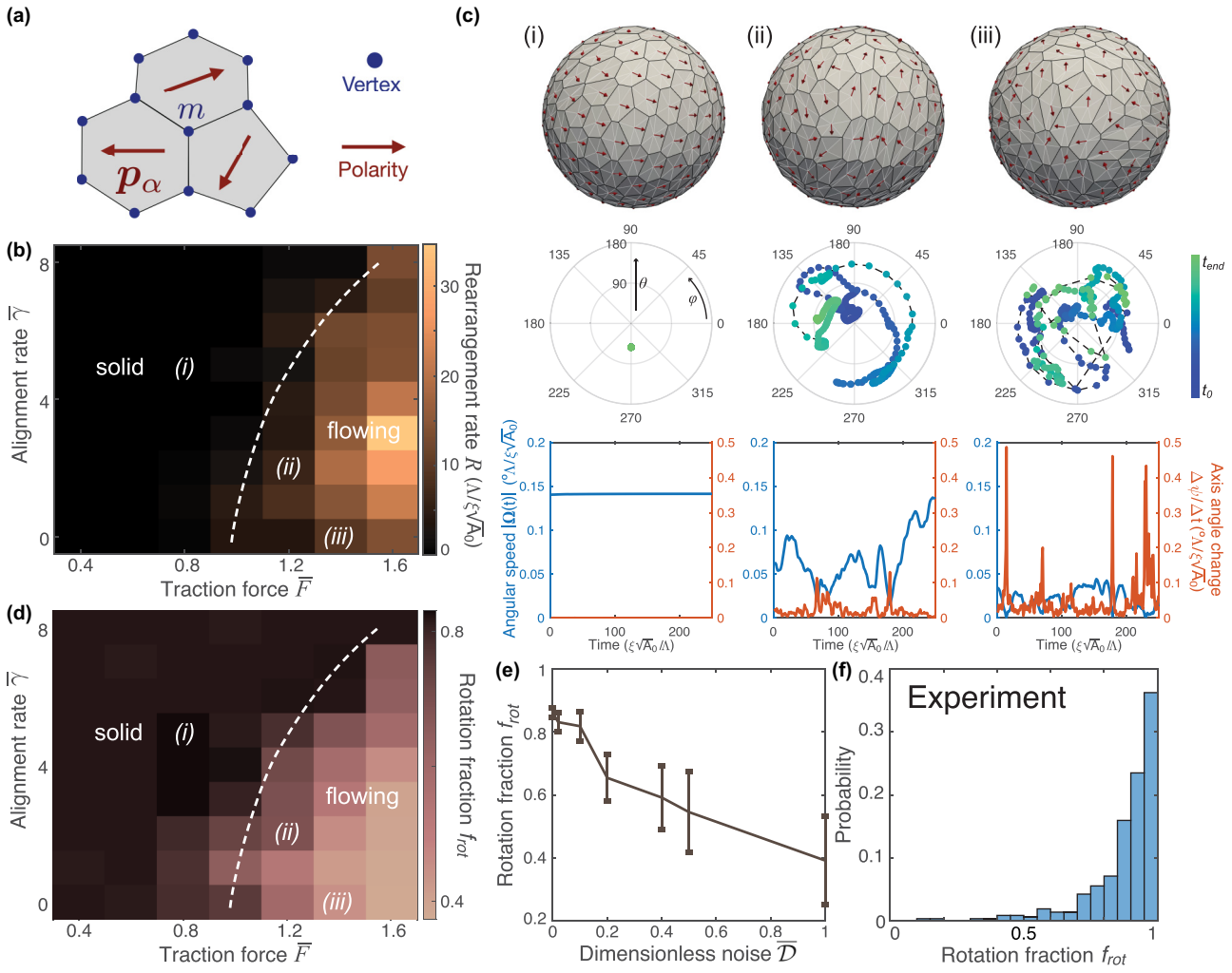

FIG. 2. Solid and flowing regimes of the active vertex model. (a) Schematic of the active vertex model. Cells are represented as polygons with vertices subjected to forces from the vertex model work function and the polarity-directed active forces. (b) Dynamic phase diagram of the active vertex model, color-coded with cell-cell rearrangement rate, with a dashed line separating the solid and the flowing regimes. (c) Simulations of the active vertex model in the solid (i) and flowing (iii) regimes, and in the transition regime between the two (ii). The top row shows a single snapshot with polarity denoted by red arrows. The second row shows the angular position of the rotation axis through time in the (θ, ϕ) polar plot. The third row shows the magnitude of the angular speed and the angular change of the rotational axis. (d), (e) The solid body rotation fraction of the surface velocity $f_{\rm rot}$ (Appendix B 5 and Fig. 13) in simulations of the solid and flowing regimes of active vertex model. (f) The rotation fraction $f_{\rm rot}$ in experiments indicates that a majority of pancreas spheres rotate as an active solid. Additional data on the instantaneous rotation fraction are included in Fig. 12. Error bars in (e) are standard deviations across more than three simulation realizations with more than 300 time points per realization.

where $\boldsymbol{v}_m$ is the velocity of vertex m, and ξ is the friction coefficient with the external environment. The term $F\langle \boldsymbol{p}\rangle_m$ describes active traction forces of magnitude F exerted by the (three) cells abutting at vertex m and in the average direction of their polarities $\langle \boldsymbol{p}\rangle_m = \sum_{\langle \alpha|m\rangle} \boldsymbol{p}_\alpha/M_\alpha$, where $\boldsymbol{p}_\alpha$ and M_α are each cell's polarity and number of vertices, respectively [Fig. 2(a)]. We consider a nondeforming spherical geometry by setting $\boldsymbol{v}_m \cdot \hat{n}_m = 0$, which specifies the normal force at vertex m with magnitude f_m^n (Appendix C).

The cell polarity $\boldsymbol{p}_\alpha$ directs the active traction force exerted by the cell α on the surrounding matrix. The time evolution of cell polarity follows the dynamics:

$$\frac{D\boldsymbol{p}_\alpha}{Dt} = \gamma\langle \boldsymbol{p}\rangle_\alpha + \sqrt{2\mathcal{D}_r}\boldsymbol{\eta}(t) + \mu\boldsymbol{p}_\alpha + p_\alpha^n \hat{n}_\alpha, \qquad (3)$$

where D/Dt denotes a corotational time derivative (see Appendix C). The first term on the right-hand side of Eqs. (3) and (C7) accounts for the alignment of cell polarity with the average polarity of its M_α nearest neighbors $\langle \boldsymbol{p}\rangle_\alpha = (1/M_\alpha)\sum_{\langle \alpha'|\alpha\rangle} \boldsymbol{p}_{\alpha'}$ with a rate γ. The second term accounts for a rotational noise with a diffusion coefficient $\mathcal{D}_r$. The polarity noise $\boldsymbol{\eta}(t) = \hat{s}_\perp \eta(t)$ is perpendicular to both cell polarity and the normal vector at the cell center $\hat{s}_\perp = \hat{n}_\alpha \times \boldsymbol{p}_\alpha/|\hat{n}_\alpha \times \boldsymbol{p}_\alpha|$. The polarity noise magnitude η is a Gaussian variable with mean 0 and variance 1. The third term is used to impose $|\boldsymbol{p}_\alpha| = 1$ at each time through a Lagrange multiplier $\mu(t) = -\gamma \boldsymbol{p}_\alpha \cdot \langle \boldsymbol{p}\rangle_\alpha$. With the last term we ensure that the polarity remains in the tangent plane of the sphere by adding a normal component with the magnitude $p_\alpha^n = -\gamma\langle \boldsymbol{p}\rangle_\alpha \cdot \hat{n}_\alpha$. In this study, we initialize the tissue with the force balanced

configuration of a Voronoi diagram construction of N randomly distributed cell centers on a sphere of radius $R_s = (NA_0/4\pi)^{1/2}$, and we initialize the direction angle of cell polarity from a uniform random distribution (see Appendix C).

We first explore the vertex model dynamics on a sphere in the absence of noise by setting $\mathcal{D}_r = 0$. We identify two distinct dynamic regimes: the solid and the flowing regimes [Fig. 2(b)]. In the solid regime, cells do not rearrange. At a finite alignment rate $\gamma > 0$, the polarity vectors are globally aligned [Fig. 2(c),(i); SM Video 6] and the sphere rotates as a solid body around a constant axis, consistent with the experimentally observed rotational motion [Fig. 1(f),(i)]. In the flowing regime, cells continuously rearrange and the sphere rotation speed is significantly lower than in the solid regime [Fig. 2(c),(iii)]. We identify these regimes in a dynamic phase diagram [Fig. 2(b)] by measuring the cell rearrangement rate R. The flowing regime appears only when the active traction force magnitude F is greater than the threshold value F_c, which increases with the alignment rate γ. Near the transition, the sphere dynamics is erratic with sudden bursts of cell rearrangements occasionally punctuating the otherwise solidlike rotating state, leading to changes in the orientation of the rotation axis [Fig. 2(c),(ii); SM Video 7]. This behavior is reminiscent of the yielding transition [36], and the sphere dynamics is consistent with the rotation axis drift found in experiments [Fig. 1(g),(ii)]. In particular, for a vanishing alignment rate $\gamma = 0$, a well-defined transition exists in the steady state [38].

A key question is, which dynamic regimes do rotating pancreas spheres exhibit? Due to the high uncertainty to identify cell rearrangements in the experimental data, a reliable measurement of the rearrangement rate R was not feasible. Instead, we address this question by decomposing the surface velocity field $\mathbf{V}(\theta, \phi)$ in spherical harmonic modes (Appendix B 5 and Fig. 11). We then define the solid body rotation fraction quantity f_{rot} that captures the solid body rotation component of the full surface velocity field [Fig. 2(d)]. In our simulations in the solid regime (state i), the surface velocity $\mathbf{V}(\theta, \phi)$ has a high fraction $f_{\text{rot}} \approx 0.8$ of $l = 1$ (rotational) mode, compared to the flowing regime (state iii) with fraction $f_{\text{rot}} \approx 0.3$ of this mode. In experiments, we found that more than 80% of the time, rotating spheres have a rotation fraction $f_{\text{rot}} \gtrsim 0.8$, implying that active solid rotation is the dominant mode [Fig. 2(f), Fig. 12]. In simulation, we can affect the rotation fraction by changing the strength of noise. When we increase the noise in simulations, the rotation fraction decreases, driving the system from solid rotation to the flowing regime [Fig. 2(e)]. Further, we found that increasing the cell area stiffness brings the system closer to the solid regime (Fig. 13). Altogether, the quantitative comparisons between experiments and simulations indicate that when rotating, pancreas spheres act as active solids, with some spheres operating near the solid to flow transition showing drift in the rotation axis.

IV. POLARITY ALIGNMENT AND ACTIVE TRACTION FORCE CONTROL CELL SHAPE PATTERNS

With these insights into the mechanics of the rotating spheres, we next investigated how traction forces and tissue rotation affect cell shapes in pancreas spheres. We therefore performed single-cell segmentation [Fig. 3(a); see Appendix B 6] and quantified two key cell shape parameters in the experiments: (i) norm of the cell elongation tensor $|\mathbf{Q}|$, and (ii) cell elongation orientation angle β with respect to the azimuth in the direction of motion [Fig. 3(b)]. Note that cell shape and angle quantifications are performed in the local tangent plane of the 3D sphere. The 2D Mercator projection is provided for visualization purposes. Surprisingly, in experiments, we found that the cell shape orientation is nearly aligned system-wide [Fig. 3(c)] with the orientation angle distribution $P(\beta)$ showing a pronounced peak at either $\beta \approx 45^\circ$ or $\beta \approx 135^\circ$ [Fig. 3(d)]. In the active vertex model, when polarity alignment is turned off, the randomly oriented active traction force will in any particular realization still result in a net torque that generates a rotation. However, in this case, the rotation speed is slower and the cell shape orientation does not show a preferred angle β [Figs. 3(e) and 3(f)], and $P(\beta)$ shows a flat distribution. This distinction from experiments indicates that polarity alignment is required to generate the observed rotational dynamics in pancreas spheres.

To investigate the role of active traction forces in sphere dynamics, we focus on cell shape dynamics during rotation arrest. We found that during rotation, the cell shape elongation (as quantified by the mean cell elongation $\langle|\boldsymbol{Q}|\rangle$; see Appendix B 6) shows a maximum near the equator (polar angle $\theta = 90^\circ$), with cells at both poles being more isotropic [Fig. 3(g), blue line]. In contrast, cell elongation in nonrotating spheres is roughly spatially homogeneous [Fig. 3(g), orange line]. Interestingly, we found that as spheres stop rotating, the shape of cells becomes more isotropic, reaching a level that is comparable to cells in nonrotating spheres [Fig. 3(h), arrowhead]. Within the active vertex model, a sphere can stop rotating in two ways: (i) by turning off the active traction force, or (ii) by turning off the alignment rate. We reason that the experimental observation corresponds to case (i), since turning off alignment while keeping the active traction force constant would put the system in a mechanically frustrated state, where polarity vectors are misaligned and cells would become more stretched. Indeed, by performing the respective simulations [Figs. 3(j)–3(l)], we found that turning off the active traction force recapitulates the reduction in cell shape elongation as observed during rotation arrest in experiments. Consistent with experiments, the mean elongation of cells near the equator is higher in rotating spheres compared to nonrotating spheres [Fig. 3(j)]. Furthermore, we found that the cell orientation β exhibits a unimodal distribution during rotation (with a peak $\approx 45^\circ$), which subsequently homogenizes after rotation arrest [Fig. 3(i)]. This behavior is similarly observed in our simulation with active traction force turned off [Fig. 3(l)].

V. CHIRAL SYMMETRY BREAKING IN THE CELL SHAPE ORIENTATION FIELD

Cell morphology patterning is known to encode information about tissue mechanics during development [39] and apoptosis [6]. Remarkably, we found that the cell shape orientation angle β in rotating pancreas spheres shows a preference to be either $\approx 45^\circ$ or $\approx 135^\circ$ for a sustained period of time

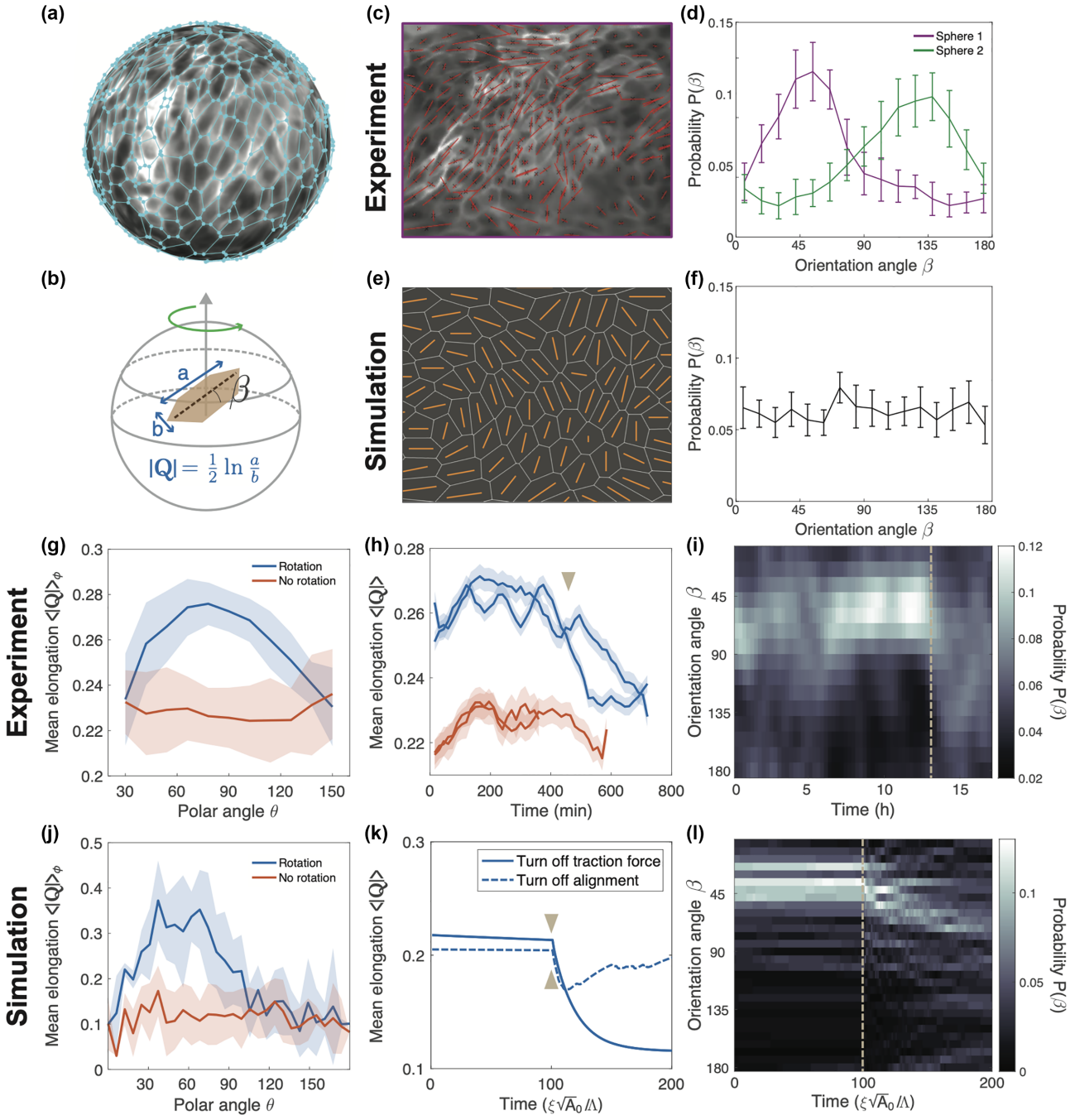

FIG. 3. Polarity alignment and active traction force control cell shape patterns. (a) Cell segmentation (cyan) performed on the projection of a pancreas sphere (gray: Myh14 signal). (b) Schematic defining cell shape elongation parameter $|\boldsymbol{Q}|$ and cell shape orientation angle β (defined with respect to azimuth). (c), (e) A Mercator projection showing the cell elongation pattern in experiments (c) and the active vertex model (without polarity alignment) (e). (d) The cell shape orientation distribution $P(\beta)$ in two different experiment spheres, showing a unimodal distribution with a peak at either 45° or 135°. (f) The cell shape orientation distribution $P(\beta)$ in the active vertex model (without polarity alignment) shows a uniform distribution. (g)–(i) Cell shape dynamics in experiments during rotation arrest. Mean cell elongation $\langle|\boldsymbol{Q}|\rangle_\phi$ (azimuthal average) as a function of polar angle θ before (blue curve) and after (orange curve) rotation arrest (g). Mean cell elongation $\langle|\boldsymbol{Q}|\rangle$ (whole system average) as a function of time for two spheres that undergo rotation arrest (blue curves, brown arrow denotes start of arrest) and two spheres that do not rotate (orange curves) (h). Probability-time kymograph of cell orientation angle β for a sphere that undergoes rotation arrest [(i), brown dotted line denotes start of arrest]. (g)–(i) The corresponding cell shape dynamics in the active vertex model during rotation arrest. In (k), we compare the mean cell elongation $\langle|\boldsymbol{Q}|\rangle$ (whole system average) when either active traction force (solid blue curve) or polarity (dotted blue curve) is turned off. In (j) and (l), we show the plots for the case when active traction force is turned off. Error bars in (d), (f), (g), and (j) are standard deviations across more than 300 data points per angular bin. Error bars in (h) are standard errors of the mean across more than 250 cells per time point.

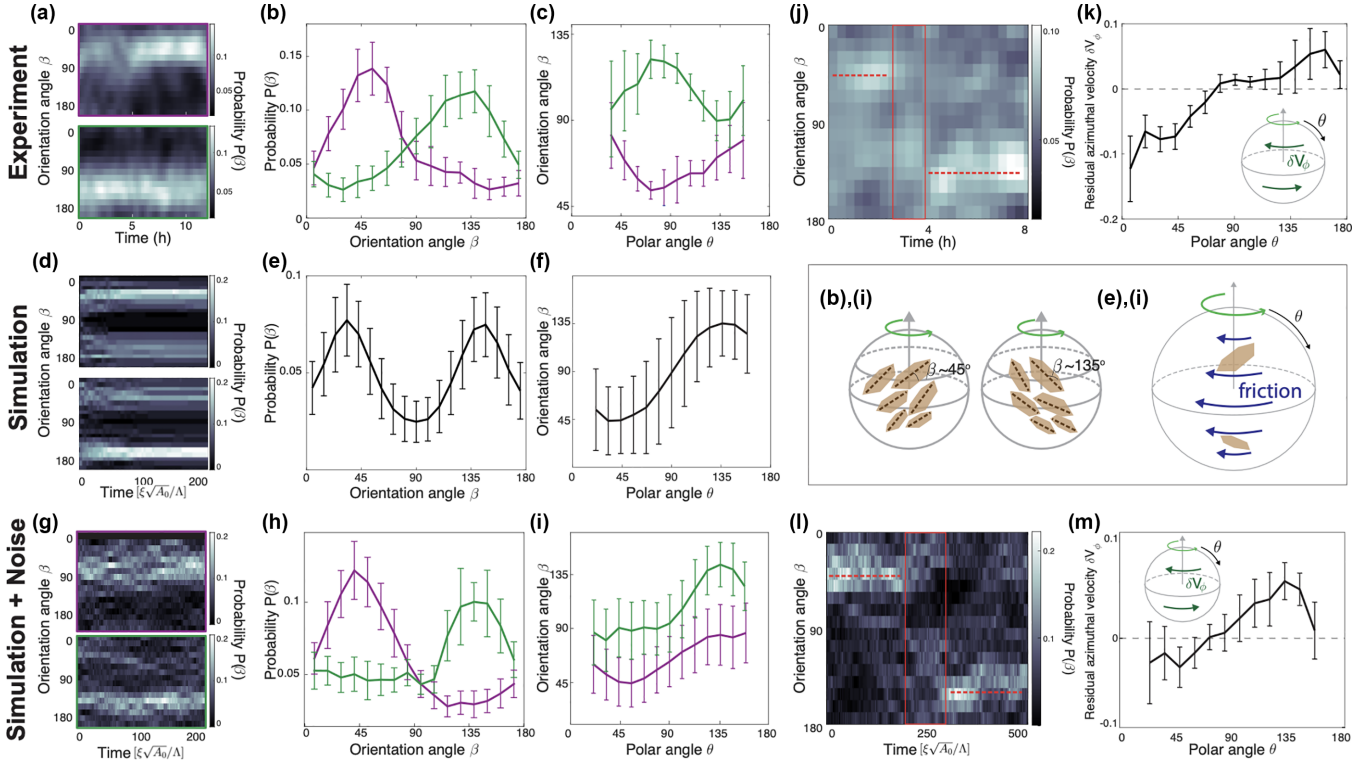

FIG. 4. Chiral symmetry breaking in the cell shape orientation field. (a) Probability-time kymograph of the cell orientation β for two different pancreas spheres undergoing persistent rotation. (b) The cell orientation probability distribution $P(\beta)$ for the two spheres in (a) shows unimodal distributions with peaks at around 45° (purple) and 135° (green). (c) Azimuthally averaged cell orientation angle $\langle\beta\rangle_\phi$ as a function of polar angle θ for the two spheres in (a). Note that β remains less (more) than 90° for the purple (green) state for the entire sphere, as illustrated in the schematic [(b),(i)]. (d)–(f) Analogous cell orientation analysis performed on simulations (without noise). $P(\beta)$ shows bimodal distribution with peaks at both 45° and 135° (e). The polar dependence of $\langle\beta\rangle_\phi$ (f) indicates that cell orientation is symmetric about the equator, as illustrated in the schematic [(e),(i)]. (g)–(i) Analogous cell orientation analysis performed on simulations (with noise). (j), (l) Probability-time kymographs of cell orientation β showing a switch of preferred angle from 45° to 135° in experiment (j) and theory (l). (k), (m) The residual azimuthal velocity $\delta\mathbf{V}_\phi$ (Appendix B 4) as a function of polar angle θ for experiment (k) and simulation (m). Insets show the directionality of $\delta\mathbf{V}_\phi$ with respect to angular velocity. All simulations in this figure have parameters $\overline{F} = 0.8$, $\overline{\gamma} = 3$, and $\overline{\mathcal{D}} = 0.2$ (for simulations with noise). Additional data are shown in Fig. 16, and comparisons between experiments and simulations are shown in Fig. 17. Error bars in (b), (c), (e), (f), and (h), (i) are standard deviations across kymographs in (a), (d), and (g), respectively ($N_t > 45$, $N > 200$ per time point, N_t = number of time points). Error bars in (k), (m) are standard deviations across kymographs marked with a red box in (j), (l), respectively ($N_t > 5$, $N \sim 1000$ per time point).

[Figs. 4(a) and 4(b)], as shown by the unimodal orientation angle distribution $P(\beta)$, which in a nonrotating sphere is distinctively uniform (Fig. 14). The cell elongation pattern also reveals a topological defect of charge +1 near each pole (Fig. 22). The rotation itself does not break the chiral symmetry. However, the additional up-down symmetry breaking of the cell elongation pattern, revealed in the asymmetry of $P(\beta)$, reveals an overall chirality of the rotating pancreas sphere. Careful reasoning reveals that up-down symmetry is also broken (Fig. 15). When we computed the mean orientation angle $\langle\beta\rangle_\phi$ (averaged azimuthally), we found that the cell orientation is roughly independent of the polar angle θ [Fig. 4(c) and Fig. 16].

To investigate the nature of this broken chiral symmetry, we turned to the active vertex model. Surprisingly, we found that in simulations, the orientation distribution $P(\beta)$ is bimodal, with peaks at both ≈45° *and* ≈135° [Figs. 4(d) and 4(e)]. One explanation for this coexistence of both orientation angles comes from the spherical geometry of the system. In solid sphere rotation, cells near the equator move faster than those near the pole, thus generating a gradient of shear stress induced by friction along the polar direction θ [Fig. 4(e),(i)]. This could in principle result in shear alignment of the cell elongation axis, which has been shown to behave as a nematic director. Such a mechanism would predict a symmetric cell orientation profile along the equator, with cell orientation predominantly taking the value of ≈45° at the "northern" hemisphere ($\theta < 90°$) and ≈135° at the "southern" hemisphere ($\theta > 90°$) [Fig. 4(e),(i)]. Indeed, the measured orientation angle β from simulations shows the expected θ dependence [Fig. 4(f)].

While the spherical geometry provides an explanation for the existence of two preferred angles, it does not explain how the symmetry is broken in experiments. The symmetric cell shape orientation profile in simulations [Figs. 4(d)–4(f)] involves an abrupt change in cell elongation orientation, which generically costs elastic energy. We posit that stochastic noise in experiments could help bias cell orientation to minimize this large bending energy. By introducing a noise term into the polarity equation of the active vertex model (see Appendix C),

we found that the symmetry does indeed get broken and the orientation angle distribution $P(\beta)$ becomes unimodal with peaks at either $\approx 45^\circ$ or $\approx 135^\circ$ [Figs. 4(g)–4(i)]. This result suggests that the cell orientation field is mechanically poised in a bistable state, and it can thus be pushed into either state through stochastic noise. Indeed, in longer simulations, we found that the cell orientation β can switch between the two states [Fig. 4(l)]. During this window of switching, we detected a counterclockwise twist in the residual azimuthal velocity $\delta \mathbf{V}_\phi$, which generates the required shear gradient to flip the preferred orientation β from 45° to 135° [Fig. 4(m)]. Such a switch is also observed in experiments, with the expected residual azimuthal velocity profile [Figs. 4(j)–4(k)]. Furthermore, in both experiment and simulation, we observed the opposite switch in preferred angle from 135° to 45° (Fig. 17).

By systematically increasing the magnitude of the polarity rotational noise $\mathcal{D}_r$ in the vertex model, we found that the system undergoes a transition from a mirror-symmetric state with bimodal distribution $P(\beta)$ at low $\mathcal{D}_r$, to chiral states with unimodal $P(\beta)$ at larger $\mathcal{D}_r$ (Fig. 18). As the noise magnitude is increased further, the sphere switches between the two chiral states on simulation timescales such that it becomes effectively mirror-symmetric. At even higher noise, the polarity becomes randomly aligned, resulting in a uniform $P(\beta)$. This study shows that for weak rotational noise, the model indeed reveals chiral symmetry breaking, similar to that observed in experiments.

To investigate the underlying symmetry breaking mechanism, we turned to a simplified continuum model of the sphere with a polarity field generating active traction forces (Appendix D 1). This polarity field is tangential to the sphere and satisfies the dynamic equation

$$\partial_t \mathbf{p} + \mathbf{v} \cdot \nabla \mathbf{p} - \boldsymbol{\omega} \times \mathbf{p} = \Gamma \nabla^2 \mathbf{p}, \tag{4}$$

where $\mathbf{v}$ is the cell velocity field, $\boldsymbol{\omega} = \nabla \times \mathbf{v}/2$, and ∇^2 is the vector Laplace-Beltrami operator. Furthermore, we constrain $|\mathbf{p}| = 1$. This equation is the continuum limit of the vertex model polarity dynamics with neighbor alignment, with alignment strength Γ.

Since the polarity field contributes to the traction forces acting on the sphere, we also need to describe how traction forces are balanced by internal tissue stress. We describe the sphere as a continuum two-dimensional material that obeys the covariant force balance equation $\nabla \cdot \boldsymbol{\sigma} = F\mathbf{p} - \xi \mathbf{v}$, where $\boldsymbol{\sigma}$ is the in-plane stress tensor, F is the traction force, and ξ is the friction coefficient. We are interested in stress patterns that govern patterns of cell shape. For a given polarity field, we can determine the strain field describing the resulting cell deformation. We first consider the material to be elastic, such that in the steady state it rotates as a solid body with velocity $\mathbf{v}_0(\mathbf{r}) = \mathbf{r} \times \boldsymbol{\Omega}$. In this case, the steady-state polarity field is a solution of the Laplace equation $\nabla^2 \mathbf{p} = \mathbf{0}$. We find axis-symmetric solutions of the form $\mathbf{p} = \sin a_0 \hat{\boldsymbol{\theta}} + \cos a_0 \hat{\boldsymbol{\phi}}$, where a_0 is the angle relative to the azimuthal direction $\hat{\boldsymbol{\phi}}$ (see Appendix D), which include two topological defects at the poles as required by the Poincaré-Hopf theorem. Figures 5(a)–5(c) show examples of $a_0 = 0$, $a_0 > 0$, and $a_0 < 0$. Note that for nonzero a_0 the polarity pattern has a broken chiral symmetry, and the two topological defects differ in that they represent a source and a sink of the polarity pattern ($\mathbf{p}$ pointing outward and inward with respect to the defect). In the absence of cell rearrangements, the sphere behaves as an elastic sheet. Therefore, we determine the elastic strain field, which is related to the magnitude and orientation of cell elongation in the organoid and the vertex model. We show the strain pattern as ellipses at several polar angle values θ in Figs. 5(a)–5(c) (see also Fig. 19). Figure 5 also shows the distribution of angles β between the cell elongation axis and the azimuthal direction, and we find that despite the chirality of the polarity field, the orientation distribution of the strain field, quantified by the strain orientation angle, is mirror-symmetric with respect to 90° (see Fig. 5). Therefore, even though the polarity pattern is chiral, the cell shape pattern is not. This is consistent with the observed symmetry of the cell elongation angle distribution in the vertex model simulations in the solid regime without noise [Figs. 4(d)–4(f)].

Pure solid body rotation corresponds to a situation in the vertex model or experiment without any cell rearrangements. Occasional cell rearrangements that relax elastic stress are characterized by an effective viscosity η. The resulting tissue shear flow corresponds to a perturbation of the rigid body velocity field. The resulting velocity field tends to be slowed down near the equator compared to the poles due to friction with the external environment. In the continuum model, we consider the lowest Fourier mode of the velocity field that perturbs the rigid body rotation but does not break the chiral symmetry $\delta \mathbf{v} = v_3 \sin 3\theta$. The shear and rotation associated with this mode alter the polarity angle, which then becomes latitude-dependent, $\mathbf{p} = \sin a(\theta)\hat{\boldsymbol{\theta}} + \cos a(\theta)\hat{\boldsymbol{\phi}}$, with $a(\theta) = a_0 + a_1 \cos\theta(1 + \sin^2\theta/2)$, where $a_1 = (2rv_3)/(3\Gamma)$ is the corotational magnitude and r is the sphere radius (Appendix D 4). Using the perturbed velocity and polarity fields to calculate traction force patterns, we find that the corresponding strain pattern is chiral, as reflected in the distribution of strain orientation angles $P(\beta)$ [Figs. 5(d)–5(f)]. This chiral pattern is consistent with the observed symmetry breaking in vertex model simulations with noise [Figs. 4(g)–4(i)], as well as the experimentally observed cell elongation patterns [Figs. 4(a)–4(c)]. Our results suggest that although the spheres rotate mostly as a solid body, they operate close to a solid to flow transition where occasional rearrangements give rise to flows. Convection and corotational effects of these flows perturb the polarity field such that the chirality of the cell polarity field, stemming from the existence of two different topological defects at the poles, is revealed in the cell elongation pattern (Fig. 19). To validate this finding experimentally, we inferred traction forces for two spheres which exhibit opposite chirality (see Appendix E, Fig. 20). Indeed, we find that the two spheres with opposite chirality display opposite patterns of traction forces near the poles [Figs. 5(j) and 5(k)], consistent with our theory [Figs. 5(h) and 5(i)]. This is further confirmed by polarity patterns of chiral states in vertex model simulations (Fig. 21).

VI. DISCUSSION

In this work, we show how the collective organization of cells can give rise to the emergent chirality in three dimensions. Specifically, we find that pancreas spheres exhibit a

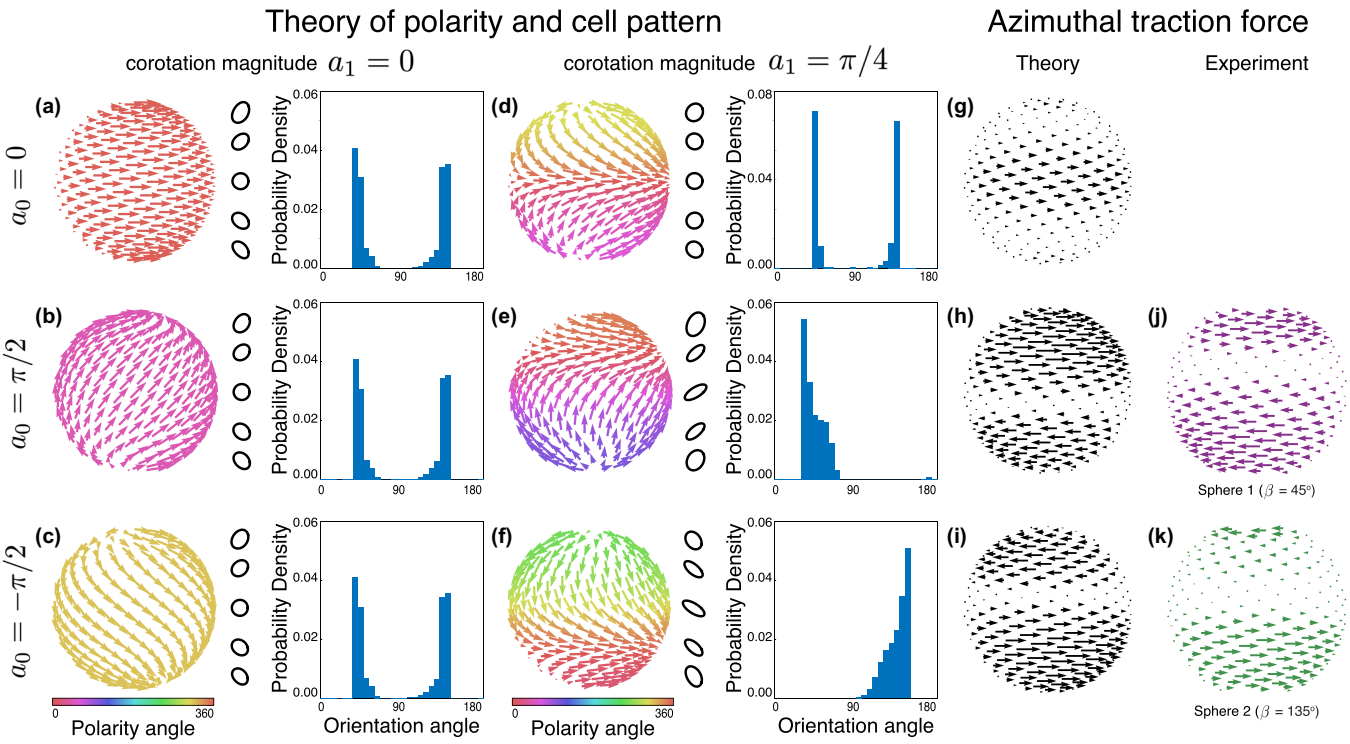

FIG. 5. Polarity patterns perturbed by corotation effects account for chiral symmetry breaking. (a)–(f) Steady-state, axisymmetric polarity field solutions to the continuum model with polarity field $\mathbf{p} = \sin a_0 \hat{\boldsymbol{\theta}} + \cos a_0 \hat{\boldsymbol{\phi}}$ without (a)–(c) and with (d)–(f) corotation effect (see Appendix D 1). The ellipses indicate cell shape and cell elongation at polar angles $\theta = \{\pi/6, \pi/3, \pi/2, 2\pi/3, 5\pi/6\}$. (g)–(i) Traction force pattern corresponding to the three polarity patterns in (d)–(f). (j), (k) Experimentally inferred traction force in the ϕ direction, for two spheres. Note that the traction force includes contributions from both cell polarity and frictional forces.

chiral symmetry breaking during active rotations, revealed by cell elongation patterns. Using both an active vertex model and a continuum theory, we show that this chirality results from an underlying chiral cell polarity pattern, which also governs the sphere rotation. Chirality of the polarity field implies an asymmetry between the two topological defects of the cell polarity field at the poles of the rotating sphere.

We find that pancreas spheres sometimes depart from solid body rotation and undergo irregular rapid changes of the orientation of the rotation axis [Fig. 1(g), Fig. 8]. The analysis of sphere rotations in an active vertex model shows that such behavior is found generally near a solid to flow transition, where the sphere is fluidized by active traction forces [Figs. 2(b)–2(d)]. The chiral pattern of cell elongation is a further signature that pancreas spheres are close to a solid to flow transition, because a purely rigid body rotation would not reveal the underlying chirality of the polarity field in the cell elongation pattern, as shown both by the vertex model [Figs. 4(g)–4(i)] and continuum theory [Figs. 5(e) and 5(f)]. Overall, our results suggest that organoid spheres organize close to a solid to flow transition controlled by active traction forces. The chirality of these forces originates from topological constraints imposed on the cell polarity vector field living on the surface of a sphere.

The process of generating tissue chirality through topological constraints is distinct from previously reported mechanisms which arise from either rotation of nodal cilia [40], chiral cell polarity [41], or a chiral phase that arises generically from a planar polarized epithelial system [42]. More generally, our results suggest an alternative route where a localized biological signal could drive symmetry breaking processes in tissues by controlling the types and locations of cell polarity topological defects. Our results are likely to be conserved in rotating spheres derived from other cell types [23,29,30,43], with potential implications for cell migration on complex 3D curved geometries, such as polarized tissue flow in *Drosophila melanogaster* [44–46].

ACKNOWLEDGMENTS

T.H.T. and M.F.S. acknowledge support from the Center for Systems Biology Dresden as ELBE Postdoctoral Fellows. A.A. acknowledges support from the Federal Ministry of Education and Research (Bundesministerium für Bildung und Forschung, BMBF) under project 031L0160. C.D. acknowledges the support of a postdoctoral fellowship from the LabEx "Who Am I?" (ANR-11-LABX-0071) and the Université Paris Cité IdEx (ANR-18-IDEX-0001) funded by the French Government through its "Investments for the Future" program. We are grateful to the Light Microscopy Facility and the Biomedical Services at the MPI-CBG for the support in all the imaging and maintenance of the mice, respectively. We thank Kinneret Keren and Anne-Kathrin Classen for stimulating discussions and comments on the manuscript.

T.H.T., A.A., and I.S.-B., contributed equally and are joint first authors.

TABLE I. Statistics for the experimental replicates (Expt.) used in paper figures, as well as the corresponding mouse lines, imaging modalities, and data analysis methods. Note that a subset of spheres (n), with the best signal-to-noise ratio, were used for full sphere surface segmentation and projection analysis (Appendix B 1). All spheres were analyzed with half-sphere surface segmentation and projection analysis (Appendix B 2), which allowed us to reveal the rotation dynamics of all the population, although with a less accurate analysis.

	Figure	Analysis	Mouse line	Imaging
Expt. 1	Fig. 8	Appendix B 2, $n = 4$		
Expt. 2	Fig. 1(f), Fig. 8	Appendix B 2, $n = 9$		
	Fig. 2(f), Figs. 4(j) and 4(k)	Appendix B 1, $n = 2$	ROSAmTmG	Light sheet
Expt. 3	Fig. 8	Appendix B 2, $n = 3$		Viventis LS1
	Fig. 2(f)	Appendix B 1, $n = 2$		
Expt. 4	Fig. 8	Appendix B 2, $n = 8$		
Expt. 5	Figs. 1(a), 1(e), 1(f), Fig. 2(f),	Appendix B 1, $n = 6$	Myh14	Light sheet
	Fig. 3, Figs. 4(a)–4(c), Fig. 8			Viventis LS1
Expt. 6	Fig. 11	Appendix B 7, $n = 2$	ROSAmTmG	Spinning disk
				Andor Revolution

APPENDIX A: EXPERIMENTAL SETUP

1. Animal lines and permits

All experiments were performed in accordance with the German Animal Welfare Legislation ("Tierschutzgesetz") after approval by the federal state authority Landesdirektion Sachsen (license DD24.1-5131/451/8). Mice were kept in standardized specific-pathogen-free (SPF) conditions at the Biomedical Services Facility (BMS) of Max Planck Institute of Molecular Cell Biology and Genetics. Genetically modified mouse lines "Myh14 < tm3.1Rsad > /Mmjax" (Jackson Laboratory stock number 023449) and "Gt(ROSA)-26Sortm4-(ACTB-tdTomato-EGFP)-Luo(C57Bl/6NCrl;Crl)" [47] were used to follow the Myosin and cell membrane patterns, respectively.

2. Preparation of organoid culture

To generate mouse pancreas spheres, we follow the protocol developed in [31] with some modifications. Briefly, we dissect the developing dorsal pancreas and harvest progenitors cells from mice at embryonic day (E) 13.5. We obtain single cells by a combination of chemical and mechanical dissociation: we incubate with TrypLE (GIBCO-BRL, Invitrogen 12604-013) at 37° for 7 min in conical wells of 60-well mini-trays (nunc, 439225), transfer the buds into a well with fresh DMEM (Gibco 10565-018), and perform the mechanical dissociation by aspirating and ejecting the bud into 10 μL pipette tips until complete dissociation under microscopic control. Then, we pool the cells from four embryos into an Eppendorf tube in order to minimize differences due to individual processing. We dilute the cell suspension to a final concentration of 75% Matrigel (Corning Costar 356231) on ice to prevent Matrigel polymerization during the mixing process. We prepare 5 μL drops in a pretreated chamber for imaging (see 3D imaging below) and incubate the chamber at 37 °C for 30 min for the polymerization of the Matrigel. The wells are then filled with 250 μL of sphere medium [DMEM/F12 + Glutamax (Gibco 10565-018), 1% Pen/Strep (Gibco 15140-122), 10 μM Y-27632 (SIGMA), 10% Y0503-IMG B27 × 50 (ThermoFisher 17504-044), 64 ng/mL FGF2 (R&D Systems 450-33-10UG) [31]] and incubated in a humidified environment containing 5% CO_2 and 95% air at 37 °C. We replace the medium to a new sphere medium without the ROCK inhibitor (Y-27632) after 2 days and again after 4 days and image at day 5.

3. 3D live imaging of pancreas spheres

Sphere samples are placed in fluorinated ethylene propylene (FEP) bottom V-shaped chambers from Viventis previously treated as follows: we fill each well with distilled water, then replace it with 70% ethanol after 5 min; we remove the ethanol and rinse once with distilled water and let it dry under the hood for 20 min and finally under UV for 20 min. After 5 days of sphere culture, time lapse 3D imaging is initiated using the LS1 Live light sheet microscope system from Viventis. The parameters used are the following: dual illumination, 2.2 μM beam, laser 488/561, exposure 50 ms, and detection objective Nikon 25× NA 1.1. Data were analyzed over six imaging experiments using two genetic backgrounds as detailed in Table I.

APPENDIX B: DATA ANALYSIS

1. Sphere surface segmentation and projection

To obtain the projection of the surface fluorescence intensity of the pancreas spheres, we first obtain the segmentation of the sphere apical (inner) surface. This is done using the following steps: First, we train a pixel classification model using ilastik [48] to distinguish between "tissue pixels" and "background pixels" in our 3D microscopy z-stack images. Using this model, we create a 3D volume mask that identifies the voxels that represent the tissue volume. Next, we use the MATLAB function `bwboundaries` to identify the inner surface of the sphere. By performing this step for the entire

z-stack, we obtain the point cloud $S = \{\boldsymbol{p}_i\}$ that defines the inner surface of the 3D sphere. Using this point cloud, we extract the apical surface fluorescence intensity $I(x, y, z)$. To simplify downstream analysis, we make the assumption that all pancreas spheres are roughly spherical, and we project the intensity onto a sphere to obtain $I(\theta, \phi)$, using the transformation $\theta = \arctan\sqrt{x^2 + y^2}/z$ and $\phi = \arctan y/x$. Ten spheres were analyzed with this method over three experiments (Table I).

2. Half-sphere surface segmentation and projection

To be able to analyze a greater number of spheres, we used an alternative method in which we project half of the sphere (Appendix F). This was done for 25 spheres over 4 experiments (Table I). For that purpose, we first segment the sphere with the arivis Vision 4D software using the "Huang" threshold. Then, we erode the segmented object by 10 pixels and subtract it from the previous segmentation, obtaining a mask for the basolateral surface of the sphere that is used with the "Object Mask" to obtain the signal only from the basolateral part of the sphere. Then, we use the Projection Viewer to obtain the MAX projection for half of the z-stack, preventing noise from the other half of the sphere on the projection that is used for PIV analysis. The resultant half-sphere projection and the mask are then used for PIV analysis using MATLAB R2020b software. For the PIV analysis we used PIVlab with the algorithm "FFT window deformation" with four interrogation passes: pass 1 of a 100 pixel box size and 50 pixel step, pass 2 of a 50 pixel box size and 25 pixel step, pass 3 of a 25 pixel box size and 13 pixel step, and pass 4 of a 13 pixel box size and 7 pixel step. The subpixel estimator was set to "Gauss 2 × 3-point" and correlation robustness to "Extreme." The output PIV was saved as a MATLAB file for the reconstruction of the 3D tissue flow field.

3. Reconstruction of the 3D tissue flow field

To reconstruct the full 3D tissue flow field, we first perform 2D particle image velocimetry (PIV) on three different projections: the equatorial projection, the north pole projection, and the south pole projection. The equatorial projection on a 2D plane is defined by $x' = \phi$ and $y' = \phi$ (here, we use prime notation to represent the projection coordinates, while the nonprime notation represents real-space coordinates). The north and south pole projections are defined as $\phi' = \pm\phi$ and $r' = (\theta, \pi - \theta)$, respectively, where $\theta = [0, \pi/2]$ for north pole projection and $\theta = [\pi/2, \pi]$ for south pole projection. Next, we perform 2D PIV on the three projections separately, using the application PIVlab in MATLAB, developed by [49]. To reconstruct the full 3D flow fields, we stitch the PIV fields from the three different projections, using the north projection for $\theta = [0, \theta_c]$, the equatorial projection for $\theta = [\theta_c, \pi - \theta_c]$, and the south projection for $\theta = [\pi - \theta_c, \pi]$. The rationale for this stitching scheme is to use regions of PIV fields from different projections that minimize distortion. $\theta_c \approx 1$ rad is determined by considering the θ dependence of the distortion for each projection. To ensure smoothness of the stitched velocity field, we further define an overlap region of $\pm\Delta\theta$ where the velocity fields from two different projections are averaged.

4. Computation of the angular velocity $\boldsymbol{\Omega}(t)$

This section explains how we obtain the angular velocity $\boldsymbol{\Omega}(t)$ and the residual velocity from the motion of vertex model spheroids and the experimental spheres. We denote the position of each vertex of the vertex model at time t by $\boldsymbol{r}_i(t)$, and the vertex velocity is estimated as

$$\boldsymbol{v}_i(t) = \frac{\boldsymbol{r}_i(t + \Delta t) - \boldsymbol{r}_i(t)}{\Delta t}, \tag{B1}$$

where Δt is the time interval between two subsequent frames. On the other hand, for the experimental organoids, we find the positions and velocities on the surface using PIV (see Appendix B 3). In the following, we use the term "*points*" to refer to both vertices of the vertex model epithelium and also the tracked points from PIV analysis of the spheres.

We first define the average position $\boldsymbol{R}(t)$ and average velocity $\boldsymbol{V}(t)$ of the tracked points as

$$\boldsymbol{R}(t) = \frac{1}{N}\sum_{i=1}^{N}\boldsymbol{r}_i(t), \quad \boldsymbol{V}(t) = \frac{1}{N}\sum_{i=1}^{N}\boldsymbol{v}_i(t). \tag{B2}$$

In full generality, the velocity of point i can be decomposed as

$$\boldsymbol{v}_i(t) = \boldsymbol{\Omega}(t) \times [\boldsymbol{r}_i(t) - \boldsymbol{R}(t)] + \boldsymbol{V}(t) + \delta\boldsymbol{v}_i(t), \tag{B3}$$

where $\boldsymbol{\Omega}(t)$ is an angular velocity that will be computed in the following and which is defined such that $\delta\boldsymbol{v}_i(t) = \boldsymbol{0}$ if the N points are placed on a solid body with center of mass $\boldsymbol{R}(t)$, moving at velocity $\boldsymbol{V}(t)$ and rotating with angular velocity $\boldsymbol{\Omega}(t)$.

To compute $\boldsymbol{\Omega}(t)$, we define the angular momentum $\boldsymbol{\Gamma}_i(t)$ of point i as

$$\boldsymbol{\Gamma}_i(t) = [\boldsymbol{r}_i(t) - \boldsymbol{R}(t)] \times \boldsymbol{v}_i(t) - [\boldsymbol{r}_i(t) - \boldsymbol{R}(t)] \times \boldsymbol{V}(t). \tag{B4}$$

Inserting this definition into Eq. (B3) yields

$$\boldsymbol{\Gamma}_i = \boldsymbol{\Omega}(\boldsymbol{r}_i - \boldsymbol{R})^2 - (\boldsymbol{r}_i - \boldsymbol{R})[\boldsymbol{\Omega} \cdot (\boldsymbol{r}_i - \boldsymbol{R})] + (\boldsymbol{r}_i - \boldsymbol{R}) \times \delta\boldsymbol{v}_i, \tag{B5}$$

where the time dependence has been omitted for simplicity. Equation (B5) can then be rewritten in matrix form as

$$\boldsymbol{\Gamma}_i = \boldsymbol{M}_i \cdot \boldsymbol{\Omega} + (\boldsymbol{r}_i - \boldsymbol{R}) \times \delta\boldsymbol{v}_i, \tag{B6}$$

where we have introduced the moment of inertia tensor $\boldsymbol{M}_i$ of point i,

$$\boldsymbol{M}_i = (\boldsymbol{r}_i - \boldsymbol{R})^2\boldsymbol{I} - (\boldsymbol{r}_i - \boldsymbol{R})^T(\boldsymbol{r}_i - \boldsymbol{R}), \tag{B7}$$

with $\boldsymbol{I}$ the identity tensor. The average angular momentum is obtained as

$$\boldsymbol{\Gamma} = \frac{1}{N}\sum_{i=1}^{N}\boldsymbol{\Gamma}_i = \boldsymbol{M} \cdot \boldsymbol{\Omega} + \frac{1}{N}\sum_{i}(\boldsymbol{r}_i - \boldsymbol{R}) \times \delta\boldsymbol{v}_i, \tag{B8}$$

where $\boldsymbol{M} = \sum_i \boldsymbol{M}_i/N$ is the average moment of inertia tensor. In the case of a solid-body rotation, $\delta\boldsymbol{v}_i(t) = \boldsymbol{0}$, such that the angular velocity is simply obtained from Eq. (B8) as

$$\boldsymbol{\Omega} = \boldsymbol{M}^{-1} \cdot \boldsymbol{\Gamma}_0, \tag{B9}$$

with $\boldsymbol{\Gamma}_0 = \sum_i(\boldsymbol{r}_i - \boldsymbol{R}) \times (\boldsymbol{v}_i - \boldsymbol{V})/N$.

The residual motion $\delta \boldsymbol{v}_i(t)$ is then obtained as

$$\delta \boldsymbol{v}_i(t) = \boldsymbol{v}_i(t) - \boldsymbol{V}(t) - \boldsymbol{\Omega}(t) \times [\boldsymbol{r}_i(t) - \boldsymbol{R}(t)]. \tag{B10}$$

Note that the computation of the solid-body angular velocity $\boldsymbol{\Omega}$ requires to invert the moment of inertia tensor $\boldsymbol{M}$, and thus requires $N > 2$.

5. Vector spherical harmonics decomposition and definition of solid body rotation fraction f_{rot}

The velocity field $\mathbf{V}(\theta, \phi)$ on a sphere can be decomposed into real vector spherical harmonics (SH) modes as

$$\mathbf{V}(t, \theta, \phi) = \sum_{l=0}^{\infty} \sum_{m=-l}^{l} V_{l,m}^{(1)}(t) \boldsymbol{\Psi}_{l,m}(\theta, \phi) + V_{l,m}^{(2)}(t) \boldsymbol{\Phi}_{l,m}(\theta, \phi), \tag{B11}$$

where, for each mode (l, m), $\boldsymbol{\Psi}_{l,m} = r\vec{\nabla} Y_{l,m}$ and $\boldsymbol{\Phi}_{l,m} = \vec{r} \times \vec{\nabla} Y_{l,m}$ are the curl-less and divergence-less components of the vector spherical harmonics, respectively, and $Y_{l,m}$ are the real scalar spherical harmonics defined as

$$Y_{l,m}(\theta, \phi) = \begin{cases} sP_{l,m}(\cos\theta)\, \cos(m\phi) & \text{if } m > 0, \\ gP_{l,m}(\cos\theta) & \text{if } m = 0, \\ qP_{l,|m|}(\cos\theta)\, \sin(|m|\phi) & \text{if } m < 0, \end{cases} \tag{B12}$$

where $s = \sqrt{2}\sqrt{\frac{2l+1}{4\pi}\frac{(l-m)!}{(l+m)!}}$, $g = \sqrt{\frac{2l+1}{4\pi}}$, and $q = \sqrt{2}\sqrt{\frac{2l+1}{4\pi}\frac{(l-|m|)!}{(l+|m|)!}}$ are normalization factors. The components of the velocity field are then defined as

$$V_{l,m}^{(1)} = \frac{1}{l(l+1)} \int_{\mathcal{S}} \mathbf{V} \cdot \boldsymbol{\Psi}_{l,m} d\Omega, \tag{B13}$$

$$V_{l,m}^{(2)} = \frac{1}{l(l+1)} \int_{\mathcal{S}} \mathbf{V} \cdot \boldsymbol{\Phi}_{l,m} d\Omega. \tag{B14}$$

The fraction of solid body rotation in the surface velocity $\mathbf{V}(\theta, \phi)$ is defined as

$$f_{\text{rot}} = \frac{\sum_m \left(V_{l=1,m}^{(2)}\right)^2}{\sum_{l,m} \left[\left(V_{l,m}^{(1)}\right)^2 + \left(V_{l,m}^{(2)}\right)^2 \right]}. \tag{B15}$$

The fraction $1 - f_{\text{rot}}$ quantifies the departure of the sphere movement from a solid body rotation. We use it as a measure of the tissue flow rate mediated by cell rearrangements.

6. Single-cell segmentation and quantification

To obtain the single-cell shape quantification, we first perform segmentation of the pole projections using the automated segmentation package EPySeg [50]. Once the cell boundaries are identified, the MATLAB function `regionprops` is used to find regions corresponding to single cells and to calculate their geometrical properties. Each cell region is fitted with an ellipse that has the same normalized second moments as the region. The cell elongation is defined as $Q = \frac{1}{2} \ln \frac{a}{b}$, where a and b are the lengths of the major and minor axes, respectively. The cell orientation β is defined as the angle between the major axis and the local latitude (i.e., the $\hat{\phi}$ direction). Cell area is then measured using MATLAB function `regionprops`, and the subsequent tracking is performed manually.

7. Quantifying Matrigel viscoelasticity using microrheology

To quantify the viscoelasticity of Matrigel, we performed microrheology experiments. We embedded 1 μm fluorescent beads (Invitrogen™ FluoSpheres™ Carboxylate-Modified Microspheres F8823) diluted 1:1000 in a 5 μL 75% Matrigel dome as a control. At the same time, to check if the surrounding environment has an impact on the traction forces from the spheres, we prepared another Matrigel dome, containing the beads at the same concentration, mixed with the pancreas progenitor cells that form the spheres. The preparation of the samples is as in Appendix A 2, with the difference being the sample holder, which in this case was Ibidi μ-Slide 8-Well slide (80826), and the imaging, done with a spinning disk microscope (Andor Revolution WD Borealis Mosaic; 30×/1.08 U Plan SApo, Silicone, OLYMPUS objective; XY pixel size of 0.395 μm; 10 min time interval; duration of 12 h). We then performed particle localization and tracking to obtain trajectories of the embedded beads. For that, we used a semiautomated pipeline (Yen Threshold Filter to binarize; watershed "Nucleus" segmentation with Threshold 1, Diameter 1 μm, and 100% split sensitivity; and tracking with Brownian motion by center of mass of the intensity channel from the beads) from ARIVIS4D software. Due to sample drift, we perform an additional step to obtain the drift-corrected position of bead i as $\vec{r}_i^{\,c}(t) = \vec{r}_i(t) - \langle \vec{r}(t) \rangle$, where $\langle \vec{r}(t) \rangle = \frac{1}{N} \sum_j \vec{r}_j(t)$ is the mean positions of beads within a 10 μm radius. The drift-corrected mean-squared displacement (MSD) is then calculated as $\text{MSD}(\tau) = \langle |\vec{r}_i^{\,c}(t+\tau) - \vec{r}_i^{\,c}(t)| \rangle_t$, where $\langle \cdots \rangle_t$ denotes averaging over all time frames.

APPENDIX C: ACTIVE VERTEX MODEL ON A SPHERE

We consider a two-dimensional vertex model with cell polarity on a rigid sphere. Cells on the sphere are represented as polygons that are outlined by straight edges connecting vertices [34]. We consider a polygonal cell network consisting of N_{c} cells labeled α, N_{v} vertices labeled m, and N_{b} straight bonds between connected vertices labeled $\langle mn \rangle$, where m and n are the vertices they connect. Each cell is characterized in terms of its area A^α, perimeter L^α, and polarity $\boldsymbol{p}_\alpha$.

In our vertex model, the forces stemming from the mechanical properties of individual cells and from the interactions between them originate from the vertex model work function

$$W = \sum_{\alpha \in \text{cells}} \frac{1}{2} K^\alpha \left(A^\alpha - A_0^\alpha\right)^2 + \sum_{\alpha \in \text{cells}} \frac{1}{2} \Lambda^\alpha L^\alpha. \tag{C1}$$

The first term describes an area elasticity contribution, with A_0^α the preferred cell area and K^α the area stiffness. The second term describes a contribution due to the tension of network bonds, where Λ^α is the perimeter tension magnitude, and L^α denotes the cell perimeter [34,37]. Here, for simplicity, we consider the case in which the cell parameters are identical for all cells in the tissue: $K^\alpha = K$, $A_0^\alpha = A_0$, and $\Lambda^\alpha = \Lambda$. Due to the spherical geometry, polygonal cells are not coplanar, and a unique definition of cell area requires a suitable triangulation. Here, we define the cell center $\boldsymbol{X}_{\text{c}}$ as the average position of vertices, and we triangulate each cell by connecting the cell center to consecutive cell vertices $\boldsymbol{X}_i$ and $\boldsymbol{X}_{i+1}$ in counterclockwise order (see Fig. 6). Hence, for a given cell, we obtain

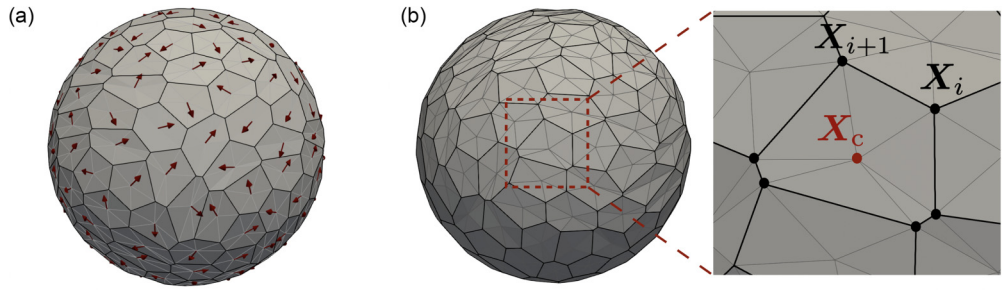

FIG. 6. (a) Example of an initial condition of the tissue configuration and of the cell polarities. (b) Tissue triangulation and definition of geometric quantities.

the cell area and perimeter as

$$A = \frac{1}{2}\sum_{i=1}^{M} |(\boldsymbol{X}_i - \boldsymbol{X}_c) \times (\boldsymbol{X}_{i+1} - \boldsymbol{X}_c)|, \tag{C2}$$

$$L = \sum_{i=1}^{M} |\boldsymbol{X}_{i+1} - \boldsymbol{X}_i|, \tag{C3}$$

where M is the number of vertices of the cell, and with $\boldsymbol{X}_{M+1} \equiv \boldsymbol{X}_1$.

At each vertex m located at position $\boldsymbol{X}_m$, force balance reads

$$\xi \boldsymbol{v}_m = \boldsymbol{f}_m^{\text{active}} - \frac{\partial W}{\partial \boldsymbol{X}_m} + f_m^n \hat{\boldsymbol{n}}_m, \tag{C4}$$

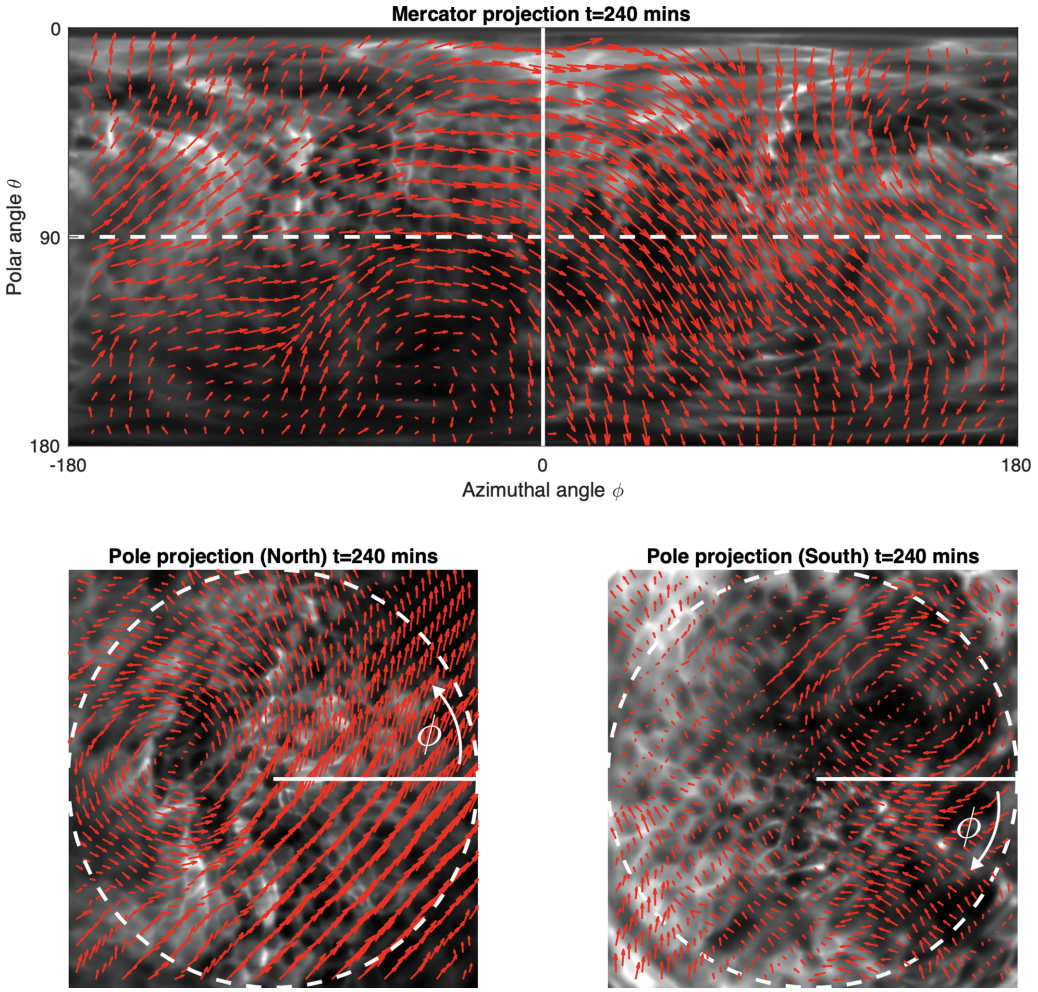

FIG. 7. Particle imaging velocimetry (PIV) field on the Mercator and pole projections. To obtain the surface velocity field $\mathbf{V}(\theta, \phi)$ at any particular time point t, we performed PIV on three different projections: (i) Mercator projection (top), (ii) "north" pole projection (bottom left), and (iii) "south" pole projection (bottom right). The PIV fields (red arrows) from the three different projections are then stitched together to minimize distortion introduced from different projections. The dotted white line is defined by $\theta = 90^\circ$ (the "equator"). The solid white line is defined by $\phi = 0^\circ$ (the "meridian"). See Appendix B 2 for more details.

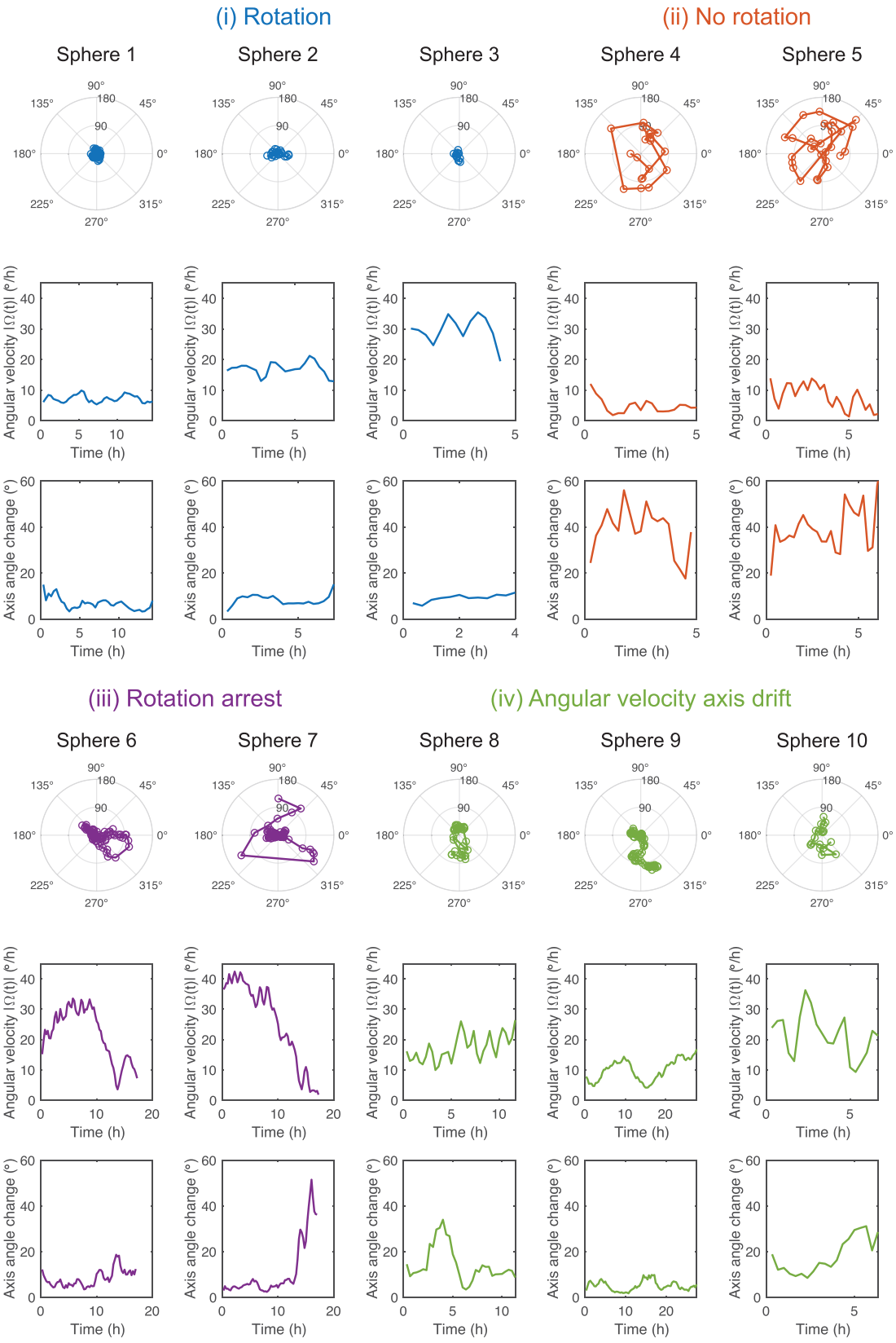

FIG. 8. Characterization of rotational dynamics of individual pancreas spheres. There are four distinct types of rotational dynamics observed in experiments: (i) persistent rotation, (ii) no rotation, (iii) rotation arrest, and (iv) rotation axis drift. The first row shows the angular position of the rotation axis in the (θ, ϕ) polar plot. The second and third rows show the angular velocity $|\boldsymbol{\Omega}(t)|$ and the axis angle change $\Delta\psi/\Delta t$, respectively.

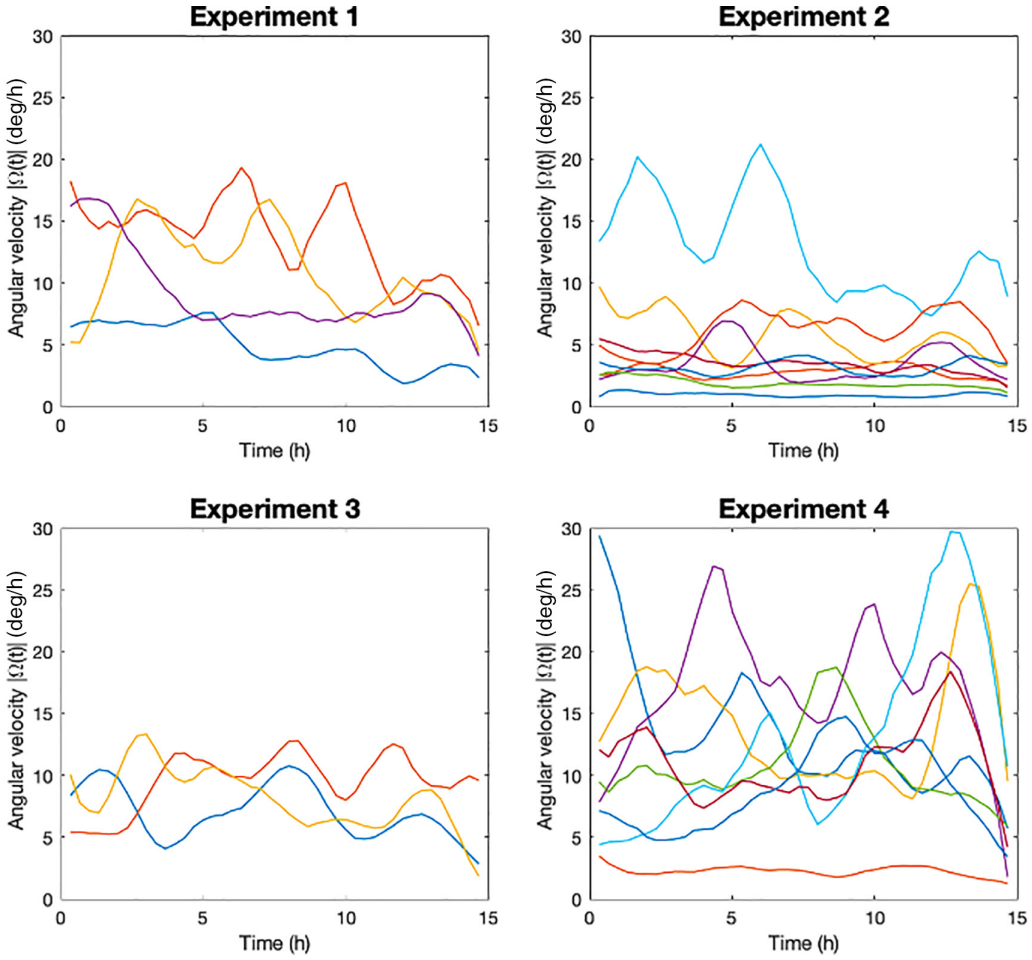

FIG. 9. Pancreas spheres exhibit distinct rotational modes within the same culture conditions. Through visual inspection of experimental videos, we found that pancreas spheres exhibit a large range of rotational dynamics, as characterized in Figs. 1(f) and 1(g). To obtain more sphere characterization, we developed a faster (but less accurate) half-sphere projection method (Appendixes B 2 and B 6) to calculate sphere rotation frequency. These plots show rotation frequencies of spheres from different experiments. We found that the spheres indeed show a large variation of dynamics that is not correlated with other spheres, even within the same experiment.

where $\boldsymbol{v}_m$ is the velocity of vertex m, and ξ is the friction coefficient with the external environment. The traction forces $\boldsymbol{f}_m^{\text{active}}$ are generated from active processes and are defined on each vertex as

$$\boldsymbol{f}_m^{\text{active}} = F \sum_{\langle\alpha|m\rangle} \frac{\boldsymbol{p}_\alpha}{M_\alpha}, \tag{C5}$$

where F denotes the traction force magnitude of a cell, the sum is over the (three) cells that share vertex m, and M_α is the number of vertices of cell α. We consider a nondeforming spherical geometry by setting $\boldsymbol{v}_m \cdot \hat{n}_m = 0$, which determines the normal force as

$$f_m^n = \left(\frac{\partial W}{\partial \boldsymbol{X}_m} - \boldsymbol{f}_m^{\text{active}} \right) \cdot \hat{n}_m, \tag{C6}$$

where $\hat{n}_m$ is the unit normal vector to the sphere at vertex m.

We consider a polarity field $\boldsymbol{p}_\alpha$ in the tangent plane that directs the traction force exerted by the cell α on the surrounding matrix. The time evolution of the polarity direction follows the dynamics

$$\frac{D\boldsymbol{p}_\alpha}{Dt} = \gamma \langle \boldsymbol{p} \rangle_\alpha + \sqrt{2\mathcal{D}_r}\boldsymbol{\eta}(t) + \mu \boldsymbol{p}_\alpha + p_\alpha^n \hat{n}_\alpha, \tag{C7}$$

where D/Dt denotes a corotational time derivative (see Appendix C 1). The first term on the right-hand side of Eq. (C7) accounts for the alignment of the polarity of cell α with the polarity of its nearest neighbors with a rate γ with the definition

$$\langle \boldsymbol{p} \rangle_\alpha = \frac{1}{M_\alpha} \sum_{\langle\alpha'|\alpha\rangle} \boldsymbol{p}_{\alpha'}. \tag{C8}$$

The second term in Eq. (C7) accounts for the rotational noise with a diffusion coefficient $\mathcal{D}_r$. The white Gaussian noise $\boldsymbol{\eta}(t) = \hat{s}_\perp \eta(t)$ is perpendicular to both cell polarity and the outward normal vector to the cell, $\hat{s}_\perp = \hat{n}_\alpha \times \boldsymbol{p}_\alpha / |\hat{n}_\alpha \times \boldsymbol{p}_\alpha|$, and it has a random magnitude η that is defined as a Gaussian variable with mean 0 and variance 1. The Lagrange multiplier $\mu(t) = -\gamma \boldsymbol{p}_\alpha \cdot \langle \boldsymbol{p} \rangle_\alpha$ imposes $|\boldsymbol{p}_\alpha| = 1$ at each time. With the last term we ensure that the polarity remains in the tangent plane by adding a normal component with the

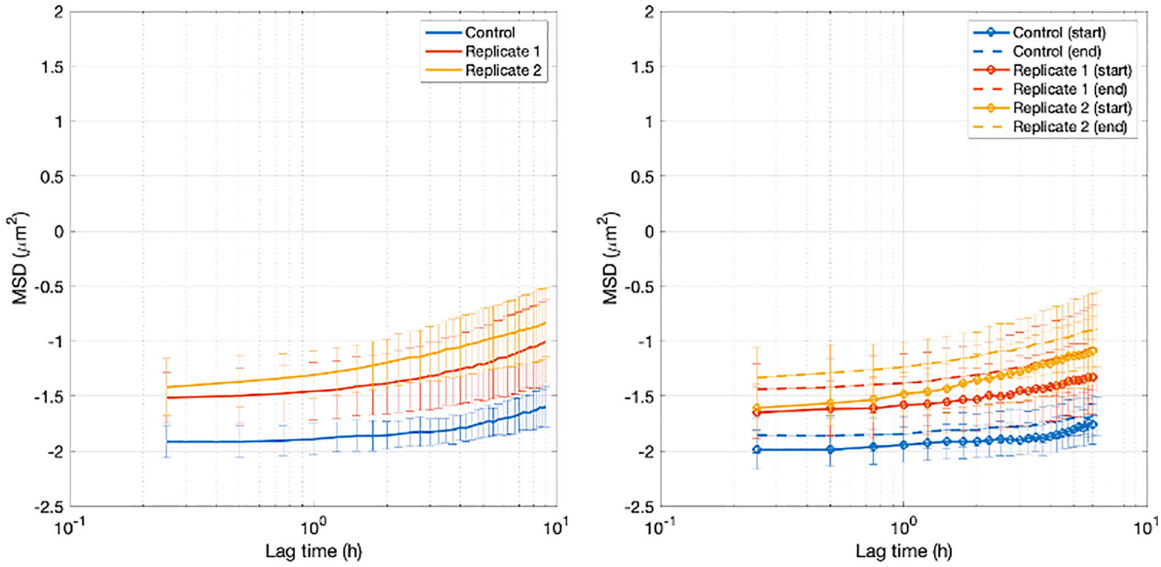

FIG. 10. Characterizing material properties of Matrigel using microrheology. We embedded beads in Matrigel with (Replicates 1 and 2) or without (Control) pancreas progenitor cells, and we computed the drift-corrected mean-squared displacement (MSD) as a function of lag time τ. We found that the MSD computed for the whole duration of the experiment ($\sim$16 h) has an exponent of roughly $\sim$0, consistent with elastic behavior (left plot). This is consistent with experiments done in Ref. [33]. Furthermore, the MSDs computed separately for the first half and second half of the experiments (right plot) are comparable, indicating that the Matrigel remains elastic and its rheological properties do not undergo significant changes.

magnitude

$$p_\alpha^n = -\gamma \langle \boldsymbol{p} \rangle_\alpha \cdot \hat{n}_\alpha. \tag{C9}$$

The dimensionless model parameters are defined as $\overline{F} = F/\Lambda$, $\overline{\gamma} = 100\gamma\xi\sqrt{A_0}/\Lambda$, $\overline{\mathcal{D}} = \mathcal{D}_r/\gamma$, and $k = KA_0^{3/2}/\Lambda$. We fix $k = 10$, which ensures mechanical stability of the cellular network as we vary the remaining parameters (except for results reported in Fig. 13, where k is varied). In this study, we initialize the tissue by a force balanced configuration of a Voronoi diagram construction of N randomly distributed cell centers on a sphere of radius $R_s = (NA_0/4\pi)^{1/2}$ with $N = 200$, $A_0 = 1$, and we initialize the cell's polarity angle from a uniform random distribution.

1. Implementation of the corotational time derivative

The cell polarities are transported with the cells through the corotational time derivative in Eq. (C7). This equation can be written for a time step Δt in a discrete form,

$$\boldsymbol{p}_\alpha(t+\Delta t) = \underline{\underline{R}}(\boldsymbol{\Omega}_\alpha \Delta t)[\boldsymbol{p}_\alpha(t) + \gamma \langle \boldsymbol{p} \rangle_\alpha \Delta t + \sqrt{2\mathcal{D}_r \Delta t}\ \boldsymbol{\eta}(t) + \mu \boldsymbol{p}_\alpha \Delta t + p_\alpha^n \hat{n}_\alpha \Delta t],$$

where the three-dimensional rotation matrix $\underline{\underline{R}}(\boldsymbol{\Omega}_\alpha \Delta t)$ rotates the polarity vector with the cell and is constructed by extracting the solid body angular velocity $\boldsymbol{\Omega}_\alpha$ of cell α from the velocity of its vertices,

$$\boldsymbol{v}_{m,\alpha}(t) = \frac{\boldsymbol{X}_{m,\alpha}(t+\Delta t) - \boldsymbol{X}_{m,\alpha}(t)}{\Delta t}, \tag{C10}$$

$$\boldsymbol{v}_{m,\alpha}(t) = \boldsymbol{\Omega}_\alpha(t) \times \boldsymbol{r}_{m,\alpha}(t) + \boldsymbol{V}_\alpha(t) + \delta \boldsymbol{v}_{m,\alpha}(t), \tag{C11}$$

where $\boldsymbol{X}_{m,\alpha}(t)$ is the position of each vertex m that belongs to cell α, $\boldsymbol{r}_{m,\alpha}(t) = \boldsymbol{X}_{m,\alpha}(t) - \boldsymbol{X}_{\alpha,\mathrm{c}}$, and $\boldsymbol{X}_{\alpha,\mathrm{c}}$ denotes the cell center position. The decomposition of velocity and the determination of the cell angular velocity follows the method described in Appendix B 4.

2. Computation of the chiral order parameter

Here, we define an order parameter to quantify the chirality of the rotating sphere using the distribution $P(\beta)$ of the cell elongation tilt angle. For each cell, we consider $\Delta\beta = \beta - \pi/2$, which is the angle relative to the local meridian. When averaged over all cells in the tissue, $\langle \Delta\beta \rangle$ is zero when $P(\Delta\beta)$ is symmetric with $P(\Delta\beta) = P(-\Delta\beta)$, corresponding to a mirror-symmetric configuration for which $\langle \Delta\beta \rangle = 0$. We observe this situation in the vertex model at low and high values of noise strength, where they correspond to a symmetric bimodal distribution and to a flat distribution $P(\beta)$, respectively. At medium magnitudes of noise strength, we observe states where the distribution $P(\beta)$ has a peak at about $\pm\pi/4$, so that $|\langle \Delta\beta \rangle| \simeq \pi/4$. These cases correspond to states with broken chiral symmetry. Therefore, we introduce the chiral order parameter of a sphere $|\langle \Delta\beta \rangle|$ and we show in Fig. 18(a) the ensemble average of this order parameter for varying noise magnitude.

APPENDIX D: CONTINUUM MODEL OF ROTATING SPHERES

1. Polarity field on a rotating sphere

We use a continuum model to describe the cell polarity by a polar field $\mathbf{p}$, as well as the cell velocity field $\mathbf{v}$ on the surface of the sphere with radius r. Both fields are constrained to be tangential to the sphere. The polarity evolves

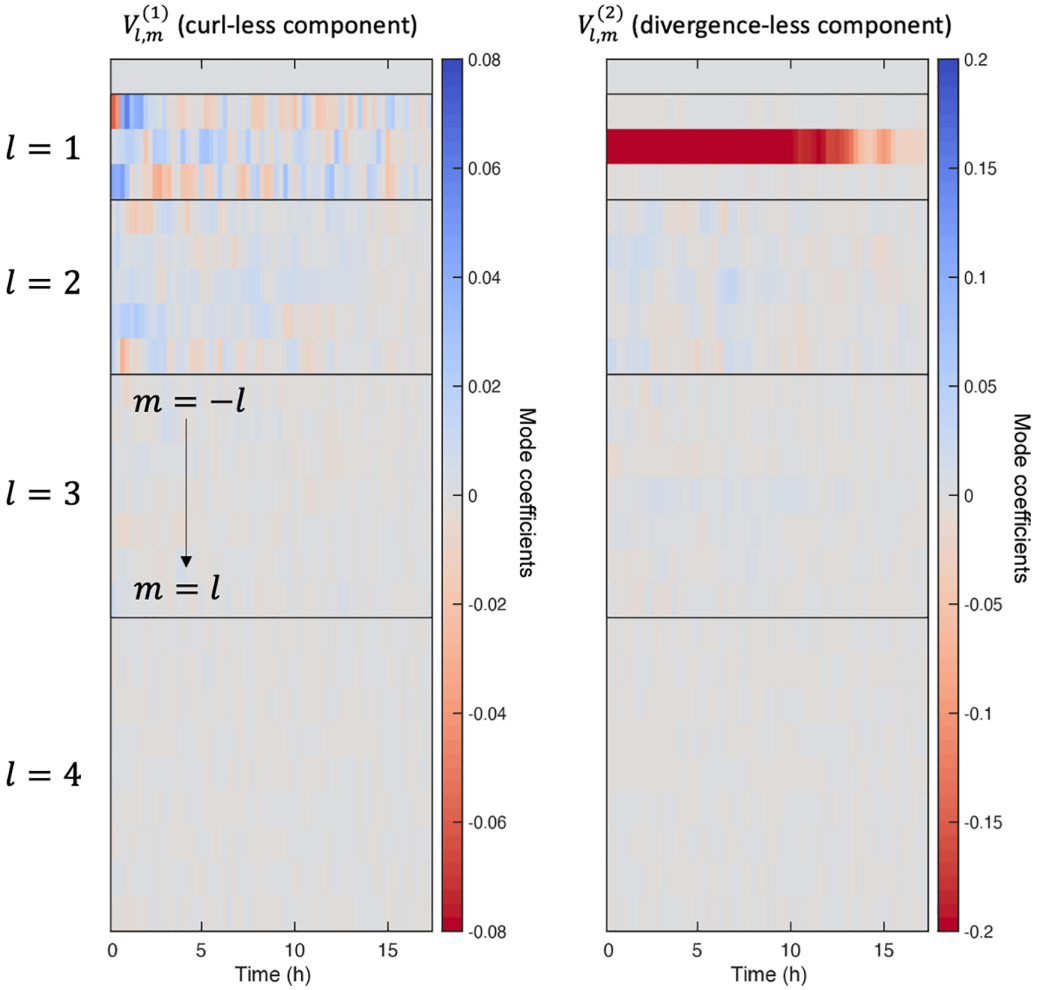

FIG. 11. Vectorial spherical harmonics mode coefficients of the velocity field. Visual representation of the mode coefficients $V^{(1)}_{l,m}$ and $V^{(2)}_{l,m}$ as a function of time, for a sphere undergoing rotation for the first ≈10 h before slowing down. As expected, the amplitude of $V^{(2)}_{l=1,m}$, which represents solid body rotation, is the dominant mode.

according to

$$\partial_t \mathbf{p} + \mathbf{v}\cdot\nabla\mathbf{p} - \boldsymbol{\omega}\times\mathbf{p} = \Gamma\nabla^2\mathbf{p}, \tag{D1}$$

where $\boldsymbol{\omega} = \nabla\times\mathbf{v}/2$ is the vorticity, ∇^2 is the vector Laplace-Beltrami operator, and Γ is the continuum limit version of polarity alignment rate γ used in the vertex model. We impose that the polarity has unit magnitude $|\mathbf{p}| = 1$ by searching for axis-symmetric steady-state solutions of the form

$$\mathbf{p} = \sin a(\theta)\hat{\boldsymbol{\theta}} + \cos a(\theta)\hat{\boldsymbol{\phi}}, \tag{D2}$$

where $a(\theta)$ is the angle between polarity and the $\hat{\boldsymbol{\phi}}$ direction, and with an axisymmetric velocity of the form

$$\mathbf{v} = v(\theta)\hat{\boldsymbol{\phi}}, \tag{D3}$$

which will be given by solid body rotation and any perturbations due to cell rearrangements. The corresponding vorticity is

$$\boldsymbol{\omega} = \frac{1}{2r\sin\theta}\partial_\theta(v(\theta)\sin\theta))\hat{\mathbf{r}} - \frac{1}{2r}v(\theta)\hat{\boldsymbol{\theta}} \tag{D4}$$

and the advection term becomes

$$\mathbf{v}\cdot\nabla\mathbf{p} = -\frac{v\cot\theta}{r}\cos a\hat{\boldsymbol{\theta}} + \frac{v\cot\theta}{r}\sin a\hat{\boldsymbol{\phi}}. \tag{D5}$$

The in-plane corotation term reads

$$-\boldsymbol{\omega}\times\mathbf{p} = \frac{1}{2r\sin\theta}\partial_\theta(v\sin\theta)(\cos a\hat{\boldsymbol{\theta}} - \sin a\hat{\boldsymbol{\phi}}) \tag{D6}$$

and the alignment term becomes

$$\nabla^2\mathbf{p} = \left(\frac{1}{r^2\sin\theta}\partial_\theta(\sin\theta\partial_\theta\sin a) - \frac{\cot^2\theta\sin a}{r^2}\right)\hat{\boldsymbol{\theta}} + \left(\frac{1}{r^2\sin\theta}\partial_\theta(\sin\theta\partial_\theta\cos a) - \frac{\cot^2\theta\cos a}{r^2}\right)\hat{\boldsymbol{\phi}}. \tag{D7}$$

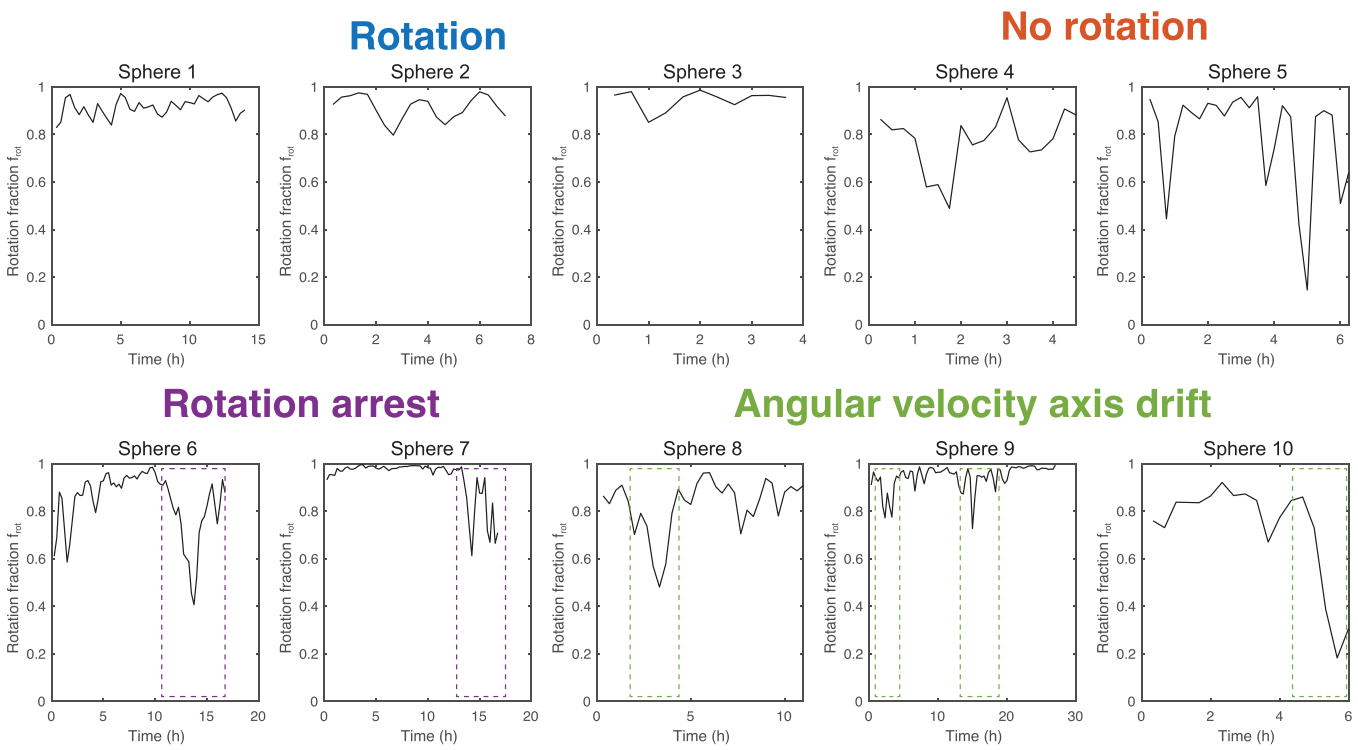

FIG. 12. Statistical characterization of solid and flowing states in experiments. To quantify the statistics of solid vs flowing states in experimental spheres, we calculate the instantaneous rotation fraction f_{rot} as a function of time for 10 different experimental spheres. We find that most of the time, spheres exhibit $f_{\text{rot}} > 0.8$. Figure 2(f) in the main text shows the distribution of f_{rot} of all measured time points for the 10 spheres shown here.

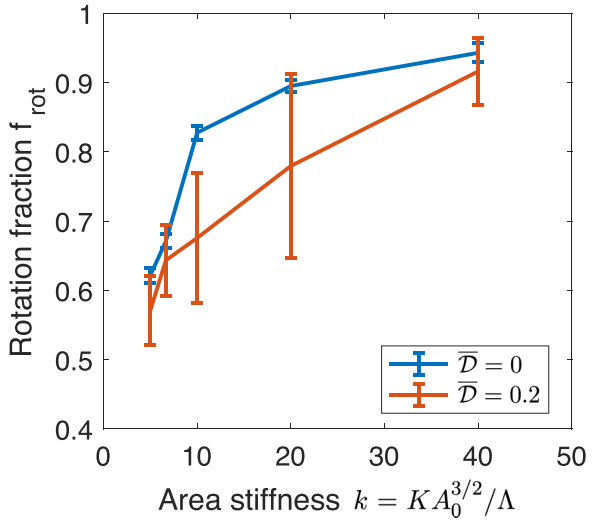

FIG. 13. Rotation fraction as a function of area stiffness with noise magnitudes $\overline{\mathcal{D}} = 0$ and 0.2. As the dimensionless parameter $k = KA_0^{3/2}/\Lambda$ increases, the area stiffness of the cellular network increases, resulting in a more solid tissue structure. Consequently, there is an increase in the rotation fraction f_{rot}. Note that below a critical area stiffness, the cellular network's shear modulus vanishes, leading to a soft network with mechanical instability. For all simulations in this figure, we fix the parameters $N = 200$, $\overline{\gamma} = 5$, and $\overline{F} = 0.8$.

At steady state, we have

$$0 = \frac{1}{r^2}\Big[[-(a')^2 - \cot^2\theta]\sin a + \Big(a'' + a'\cot\theta - \frac{r}{2\Gamma}[v' - v\cot\theta]\Big)\cos a\Big]\hat{\boldsymbol{\theta}} + \frac{1}{r^2}\big[[-(a')^2 - \cot^2\theta]\cos a - \Big(a'' + a'\cot\theta - \frac{r}{2\Gamma}[v' - v\cot\theta]\Big)\sin a\Big]\hat{\boldsymbol{\phi}} + \mu\mathbf{p}, \tag{D8}$$

where $a' = da/d\theta$, $a'' = d^2a/d\theta^2$, and μ is a Lagrange multiplier that ensures $\mathbf{p}^2 = 1$. After imposing the constraints, we must solve

$$a''\sin\theta + a'\cos\theta = \frac{r}{2\Gamma}(v'\sin\theta - v\cos\theta). \tag{D9}$$

2. Solid body rotation

If the sphere rotates as a solid body, $v(\theta) = v_1\sin(\theta)$. In this case, Eq. (D9) becomes

$$\frac{d}{d\theta}(a'\sin\theta) = 0. \tag{D10}$$

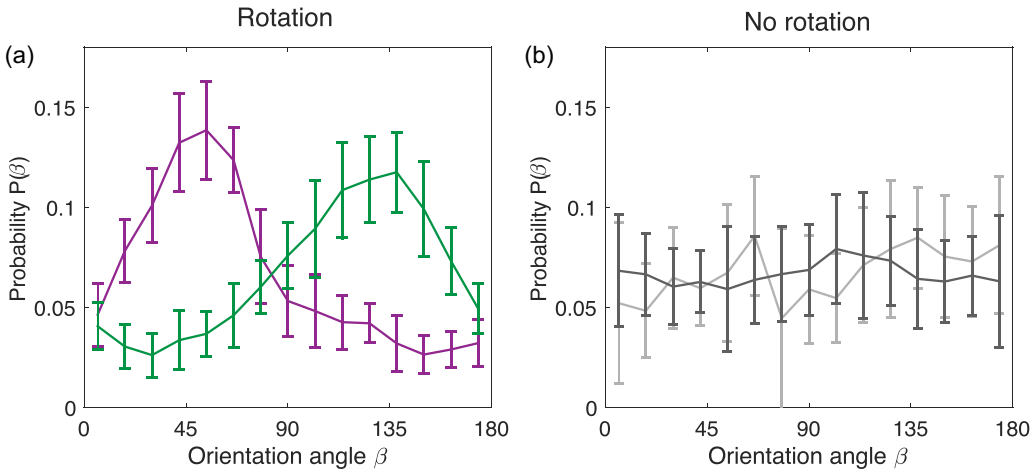

FIG. 14. Distribution of cell elongation angles $P(\beta)$ for rotating and nonrotating spheres. The cell shape orientation β in rotating pancreas spheres shows a preference to be either $\approx 45^\circ$ or $\approx 135^\circ$ for a sustained period of time. This is clearly reflected in the unimodal orientation distribution $P(\beta)$ (a). In contrast, for the nonrotating sphere, the distribution is more or less uniform (b).

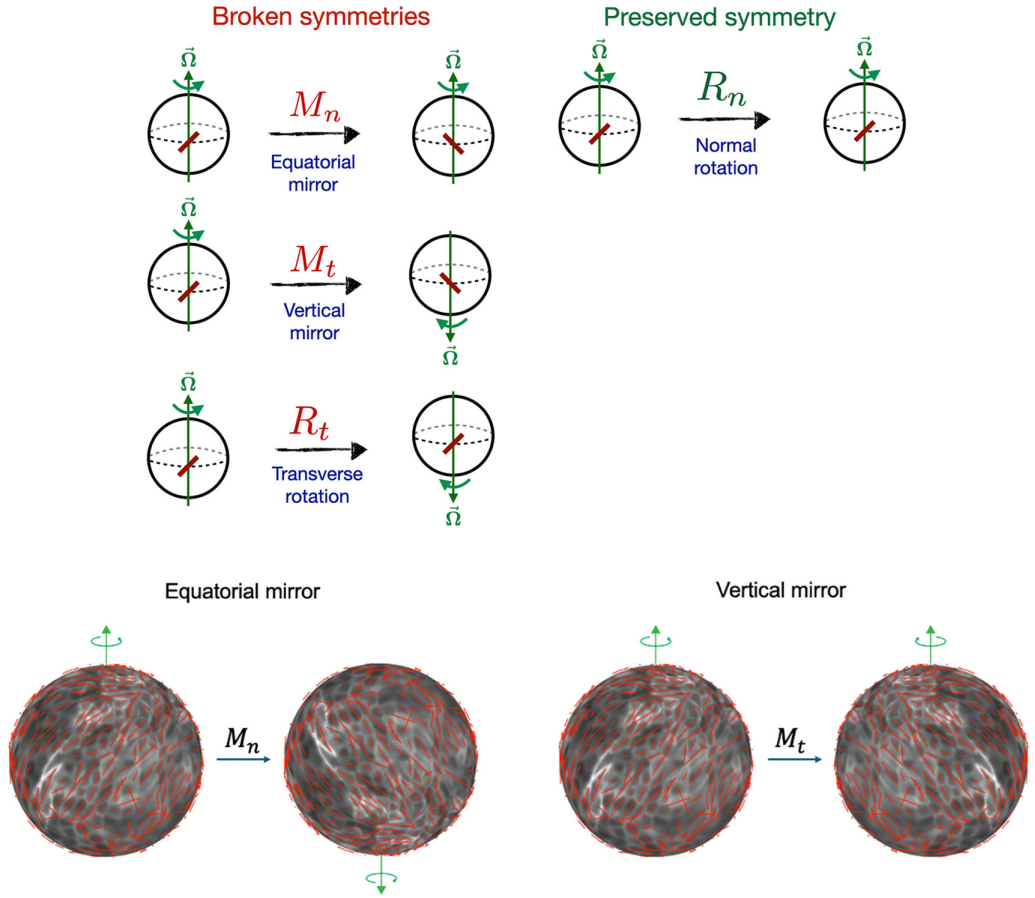

FIG. 15. Chiral and up-down symmetry breaking of the cell shape orientation field on a rotating sphere. We consider a pancreas sphere that is rotating with rotation vector $\vec{\Omega}$ around the z axis, as indicated in green. We observe that there is an average angle of cell shape orientation relative to the equation, as indicated in red. This configuration breaks several symmetries, including the following: First, an equatorial mirror operation M_n, while preserving the rotation vector $\vec{\Omega}$, mirrors the cell orientation angle. Second, a vertical mirror operation M_t inverts the rotation vector $\vec{\Omega}$ and mirrors the cell orientation angle. Third, a rotation R_t by angle π around an axis lying in the equatorial plane inverts the rotation vector $\vec{\Omega}$ while keeping the cell orientation angle invariant. Finally, this configuration is symmetric under rotations R_n around the z axis. The broken symmetry under the two mirror operations discussed (M_n and M_t) implies a chiral asymmetry for which the object cannot be superimposed on its mirror image. In particular, this means that there is no rotation that can transform a mirror image to be the same as the original. We show a snapshot of the experimental cell shape pattern and the resulting image upon performing an equatorial mirror and vertical mirror operation. Since the resulting image cannot be superimposed on the original object through any rotation, chiral symmetry is broken.

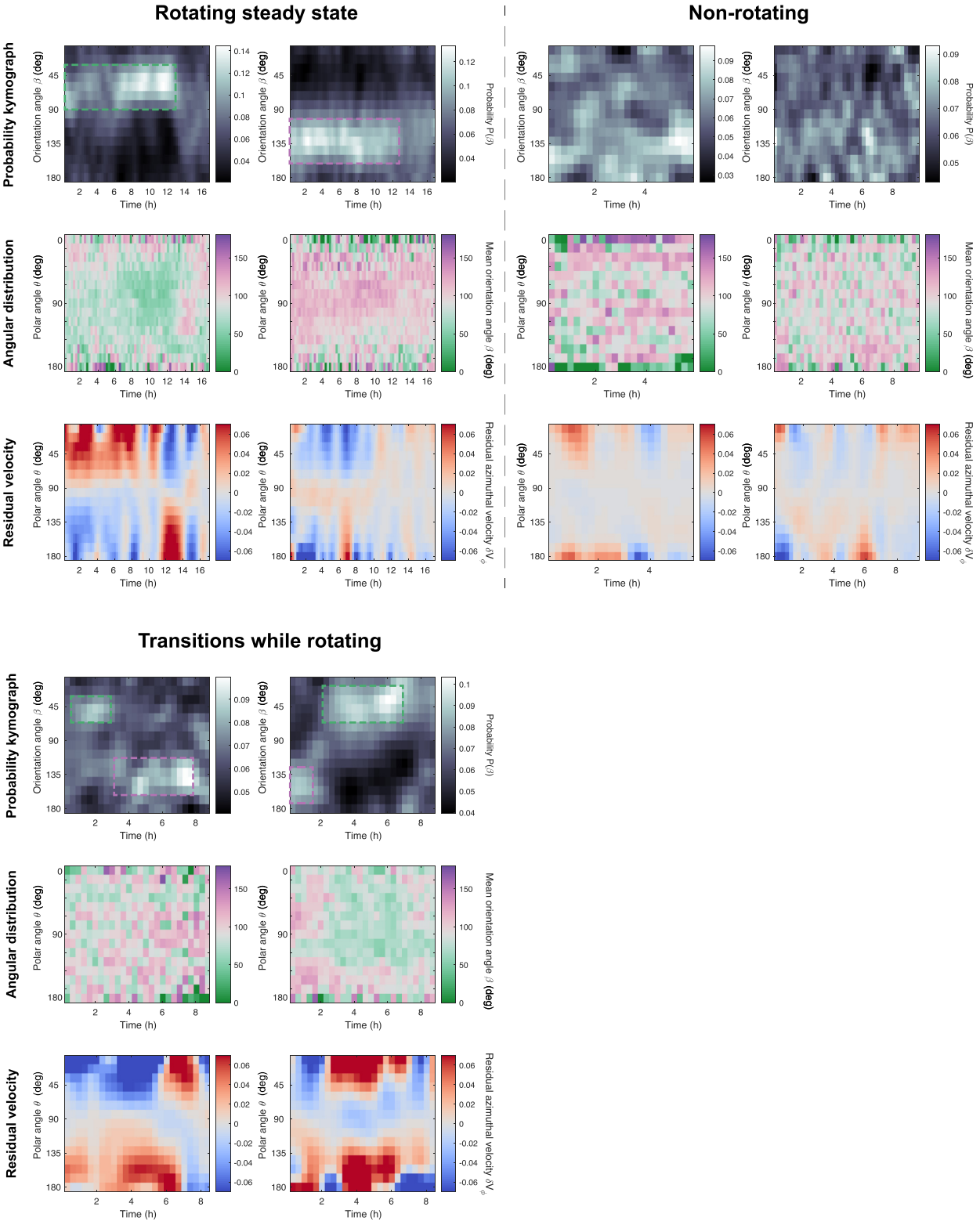

FIG. 16. Distribution of cell elongation angle $P(\beta)$ during steady-state rotation, transitional rotation, and no rotation. The first row shows probability-time kymographs of the distribution $P(\beta)$ during steady-state rotation (where the dominant tilt angle is constant), transitional rotation (where the dominant tilt angle changes), and no rotation. The second row shows azimuthally averaged cell orientation $\langle\beta\rangle_\phi(\theta)$ as a function of polar angle θ. The third row shows the residual azimuthal velocity $\delta\mathbf{V}_\phi = \delta\mathbf{V}\cdot\hat{\boldsymbol{\phi}}$ as a function of polar angle θ. For rotating spheres, we found that out of the 186 observed time points we analyzed (from four spheres), 140 time points (75%) show chiral states, with 72 and 68 time points showing prominent β peaks at 45° and 135°, respectively (51% vs 49%, purple vs green box). Time points with no prominent β peaks correspond to periods of transitional dynamics (rotation arrest or switch from one peak to another). For controls (61 time points from 2 nonrotating spheres), the distribution $P(\beta)$ is uniform [Fig. 14(b)].

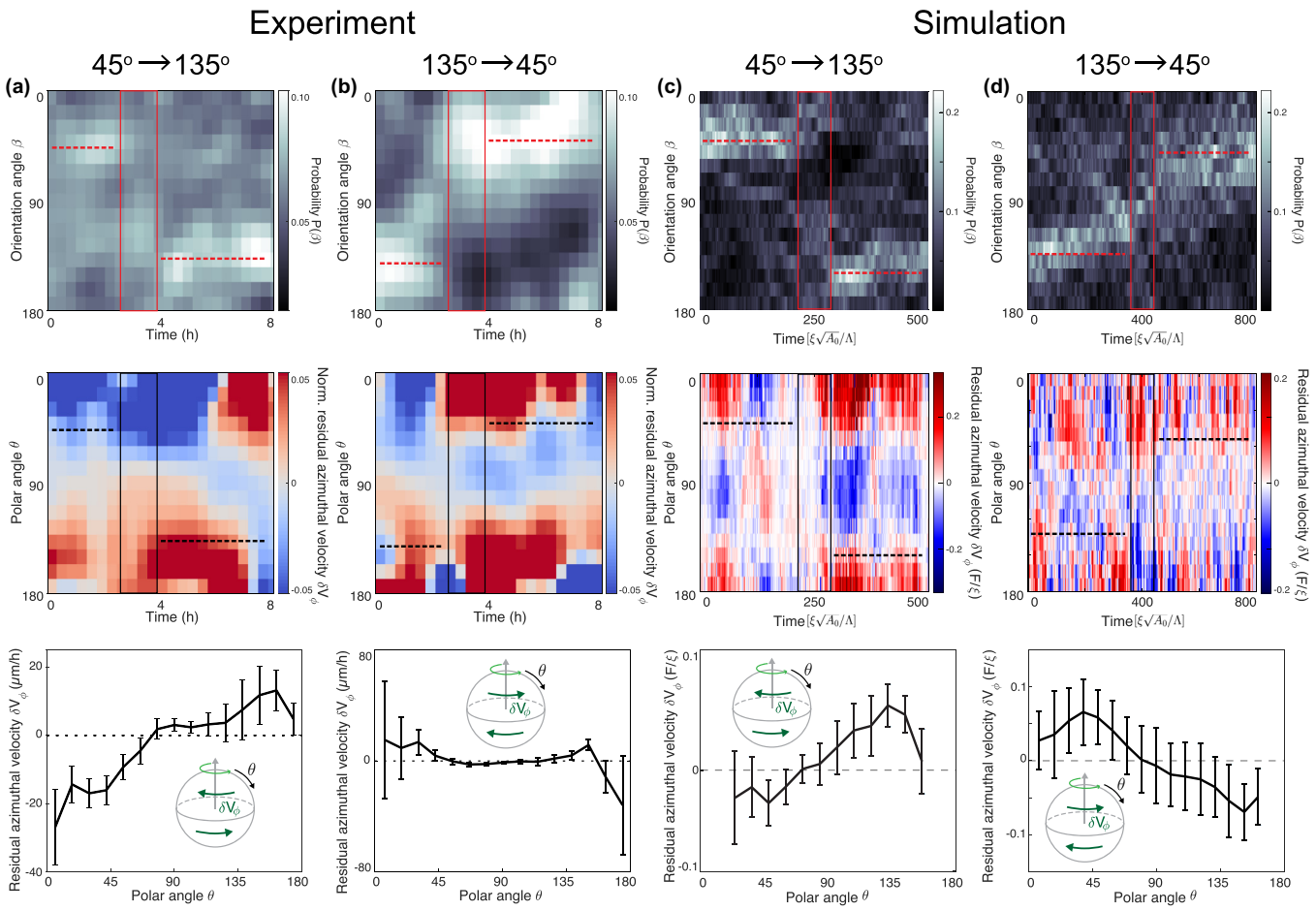

FIG. 17. Switch in cell orientation angle β in experiments and simulations. The first row shows the probability-time kymographs of cell orientation angle β showing a switch of preferred angle from 45° to 135° (a), (c) and from 135° to 45° (b), (d) in both experiments and simulation. The second row shows the probability-time kymographs for the residual azimuthal velocity $\delta\mathbf{V}_\phi = \delta\mathbf{V}\cdot\hat{\boldsymbol{\phi}}$. The third row shows the residual azimuthal velocity $\delta\mathbf{V}_\phi$ as a function of polar angle θ. Insets show the direction of $\delta\mathbf{V}_\phi$ with respect to rotation axis. In the simulations (c), (d), we fix the parameters $N = 200$, $\overline{\gamma} = 5$, $k = 10$, $\overline{F} = 0.8$, and $\overline{\mathcal{D}} = 0.2$.

We thus have $a' = b_0/\sin(\theta)$, where b_0 is an integration constant. Finally,

$$a = a_0 + b_0 \log\frac{1-\cos\theta}{1+\cos\theta}. \tag{D11}$$

We note that for $b_0 \neq 0$, the angle diverges towards the poles. We exclude this solution and set $b_0 = 0$.

The velocity magnitude v_1 is determined from the overall torque balance on the surface,

$$R\int dA\ \hat{\mathbf{r}}\times(-\nu\mathbf{p}+\lambda\mathbf{v}) = 0, \tag{D12}$$

where $\hat{\mathbf{r}}$ is a unit vector in the radial direction. Here ν describes the magnitude of active traction force in the direction $\mathbf{p}$, and λ is a friction coefficient. With $\mathbf{p} = \sin a_0\hat{\boldsymbol{\theta}} + \cos a_0\hat{\boldsymbol{\phi}}$ we thus have

$$\int_0^\pi d\theta\,\sin\theta(\nu\cos a_0 - \lambda v_1\sin\theta) = 0. \tag{D13}$$

From this we obtain the solid body rotation velocity

$$v_1 = \frac{4\nu\cos a_0}{\pi\lambda}. \tag{D14}$$

3. Velocity profiles for finite viscosity

The cell velocity field in the steady state is described by the Stokes equation with forcing,

$$\eta(\Delta_b\mathbf{v} + K\mathbf{v}) = \nabla P - \nu\mathbf{p} + \lambda\mathbf{v}, \tag{D15}$$

where Δ_b denotes the Laplace Beltrami operator on the sphere, η is a viscosity, and $K = 1/R^2$ is the Gaussian curvature. The pressure P is a Lagrange multiplier that imposes the incompressibility condition $\nabla\cdot\mathbf{v} = \mathbf{0}$. This constraint is satisfied for the axisymmetric velocity field $\mathbf{v} = v(\theta)\hat{\boldsymbol{\phi}}$. This velocity obeys the equation

$$\frac{1}{\sin\theta}\partial_\theta(\sin\theta\,\partial_\theta v(\theta)) - \frac{v(\theta)}{\sin^2\theta} + (2-\overline{\lambda})v(\theta) = -\overline{\nu}\cos a_0, \tag{D16}$$

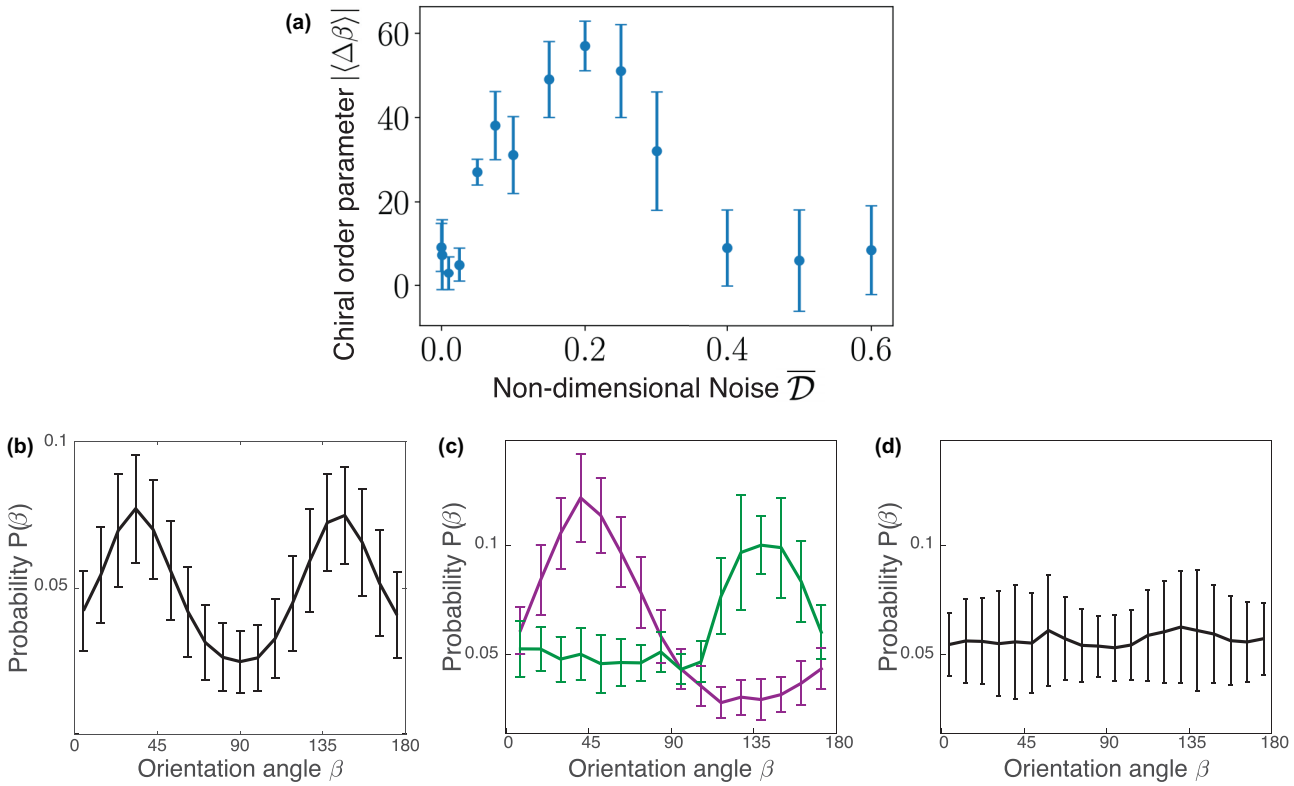

FIG. 18. Chiral order parameter as a function of noise. To investigate the role of noise in chiral symmetry breaking in the active vertex model, we vary the nondimensional noise $\overline{\mathcal{D}} = \mathcal{D}_r/\gamma$ and compute the cell orientation distribution $P(\beta)$. We then define a chiral order parameter $\langle|\Delta\beta|\rangle$, where $\Delta\beta = \beta - \pi/2$, which quantifies the asymmetry of the cell elongation angle distribution with respect to the local meridian, revealing the chiral asymmetry of the cell shape pattern. [(a), see Appendix C 2]. We found that at $\overline{\mathcal{D}} = 0$, $\langle|\Delta\beta|\rangle \sim 0$, where $P(\beta)$ is bimodal and the state is symmetric (b). At larger $\overline{\mathcal{D}}$, chiral symmetry is broken, as indicated by unimodal $P(\beta)$ [(c), $\overline{\mathcal{D}} = 0.2$]. When noise is increased further, polarity loses long-range order and the cell orientation distribution $P(\beta)$ becomes isotropic [(d), $\overline{\mathcal{D}} = 0.5$], leading to $\langle|\Delta\beta|\rangle \sim 0$. All simulations in this figure have parameters $N = 200$, $\overline{\gamma} = 5$, $k = 10$, and $\overline{F} = 0.8$.

where $\overline{\lambda} = \lambda R^2/\eta$ and $\overline{v} = vR^2/\eta$,

$$\partial_\theta^2 v(\theta) + \frac{\cos\theta}{\sin\theta}\partial_\theta v(\theta) - \frac{v(\theta)}{\sin^2\theta} + (2-\overline{\lambda})v(\theta) = -\overline{v}\cos a_0. \tag{D17}$$

We solve Eq. (D17) starting with an expansion

$$v(\theta) = \sum_{n=0}^{\infty} u_n \sin^n\theta, \tag{D18}$$

which leads to a recursion relation for coefficients,

$$u_{n+2} = \frac{n(n+1) - 2 + \overline{\lambda}}{n^2 + 4n + 3} u_n, \tag{D19}$$

with $u_2 = -\overline{v}/3\cos a_0$. The coefficient u_1 has to be determined from the torque balance. To this end, we first find an expression for coefficients u_n. We find

$$u_{2k+1} = \frac{\Gamma\left(k + \frac{3}{4} - \frac{1}{4}\sqrt{9-4\overline{\lambda}}\right)\Gamma\left(k + \frac{3}{4} + \frac{1}{4}\sqrt{9-4\overline{\lambda}}\right)}{\Gamma(1+k)\Gamma(2+k)\Gamma\left(\frac{3}{4} - \frac{1}{4}\sqrt{9-4\overline{\lambda}}\right)\Gamma\left(\frac{3}{4} + \frac{1}{4}\sqrt{9-4\overline{\lambda}}\right)} u_1, \tag{D20}$$

$$u_{2k} = \frac{3\pi}{8} \frac{\Gamma\left(k + \frac{5}{4} - \frac{1}{4}\sqrt{9-4\overline{\lambda}}\right)\Gamma\left(k + \frac{5}{4} + \frac{1}{4}\sqrt{9-4\overline{\lambda}}\right)}{\Gamma\left(\frac{3}{2}+k\right)\Gamma\left(\frac{5}{2}+k\right)\Gamma\left(\frac{5}{4} - \frac{1}{4}\sqrt{9-4\overline{\lambda}}\right)\Gamma\left(\frac{5}{4} + \frac{1}{4}\sqrt{9-4\overline{\lambda}}\right)} u_2. \tag{D21}$$

Now, we can impose torque balance from Eq. (D12) to find

$$\frac{2\overline{v}\cos a_0}{\overline{\lambda}} = \sum_{k=0}^{\infty} u_{2k+1} \frac{\sqrt{\pi}\Gamma\left(\frac{3}{2}+k\right)}{\Gamma(2+k)} + \sum_{k=1}^{\infty} u_{2k} \frac{\sqrt{\pi}\Gamma(1+k)}{\Gamma\left(\frac{3}{2}+k\right)}. \tag{D22}$$

Using the expressions for u_n above and the fact that $u_2 = -\overline{v}/3\cos a_0$, this equation directly provides the value of u_1.

Although the expansion in Eq. (D18) was convenient to solve the equation for $v(\theta)$, powers of $\sin\theta$ are not an orthonormal basis. We therefore now expand the velocity field

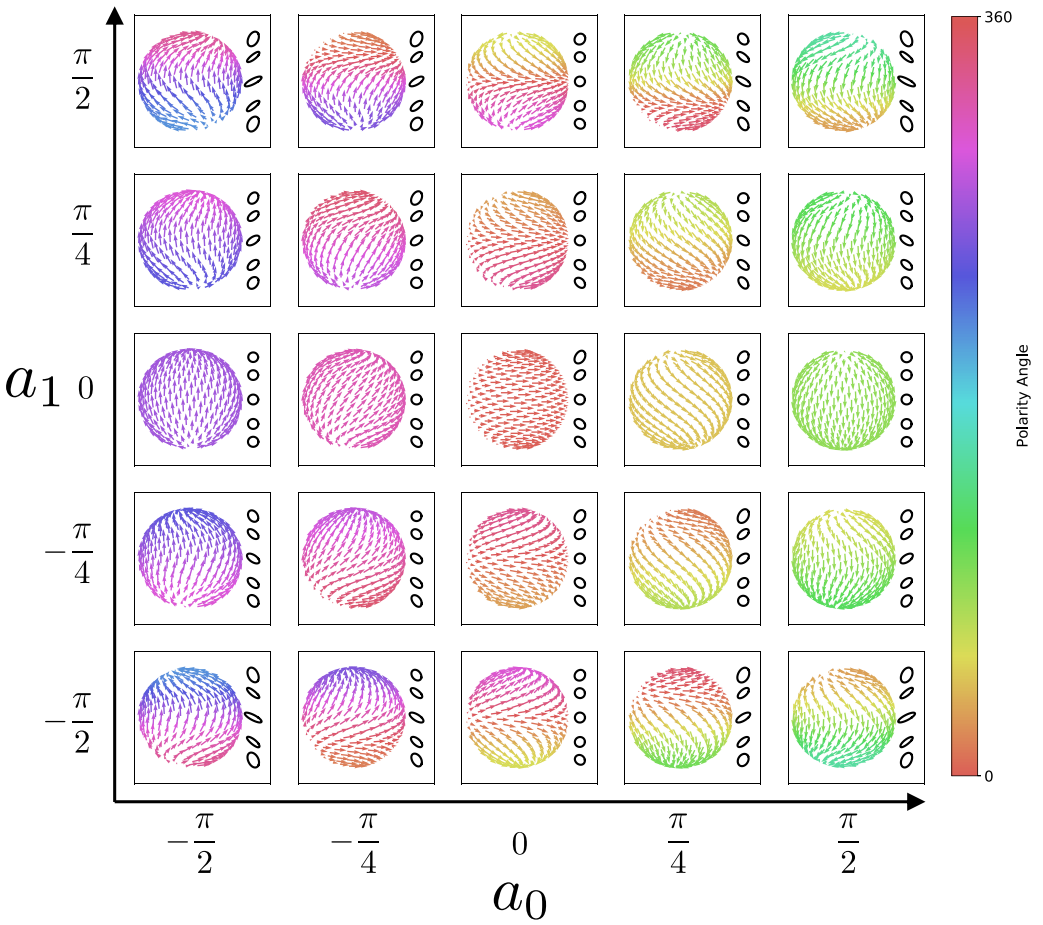

FIG. 19. Example steady-state solutions from the continuum model. Solutions of the steady-state polarity field of the form $\boldsymbol{p} = \sin a(\theta)\hat{\boldsymbol{\theta}} + \cos a(\theta)\hat{\boldsymbol{\phi}}$, where $a(\theta) = a_0 + a_1 \cos\theta(1 + \frac{1}{2}\sin^2\theta)$, for varying a_0 and a_1. The arrow color indicates the angle $a(\theta)$. Inset: shapes of deformed circles at positions on the sphere. The cell shape orientation β only breaks chiral symmetry when $a_0 \neq 0$ and $a_1 \neq 0$.

in Fourier modes,

$$v(\theta) = \sum_{m=1}^{\infty} v_m \sin(m\theta). \tag{D23}$$

The first Fourier mode corresponds to the solid body rotation. Furthermore, the velocity field is symmetric with respect to $\theta = \pi/2$ so that even Fourier modes vanish. Therefore, the third Fourier mode is the lowest mode that captures the effects of finite viscosity on the flow field. In particular, we project the velocity field to the first and third Fourier modes to find corresponding coefficients

$$v_1 = \frac{2}{\sqrt{\pi}} \sum_{k=0}^{\infty} u_{2k+1} \frac{\Gamma\left(\frac{3}{2}+k\right)}{\Gamma(2+k)} + \frac{2}{\sqrt{\pi}} \sum_{k=1}^{\infty} u_{2k} \frac{\Gamma(1+k)}{\Gamma\left(\frac{3}{2}+k\right)}, \tag{D24}$$

$$v_3 = -\frac{2}{\sqrt{\pi}} \sum_{k=0}^{\infty} u_{2k+1} k \frac{\Gamma\left(\frac{3}{2}+k\right)}{\Gamma(3+k)} - \frac{2}{\sqrt{\pi}} \sum_{k=1}^{\infty} u_{2k} \left(k - \frac{1}{2}\right) \frac{\Gamma(1+k)}{\Gamma\left(\frac{5}{2}+k\right)}. \tag{D25}$$

4. Polarity field at finite viscosity

We consider a truncated expansion of the velocity

$$v(\theta) = v_1 \sin\theta + v_3 \sin 3\theta, \tag{D26}$$

where $v_1 \sin\theta$ with $v_1 = \Omega r$ describes solid body rotation $\mathbf{v} = \boldsymbol{\Omega} \times \mathbf{x}$, where $\mathbf{x}$ is the position vector. The perturbation $v_3 \sin 3\theta$ is the lowest-order correction that is mirror-symmetric with respect to the equator. The equation for the polarity angle then reads

$$a'' \sin\theta + a' \cos\theta = \frac{r v_3}{2\Gamma}(3\cos 3\theta \sin\theta - \sin 3\theta \cos\theta). \tag{D27}$$

Note that the solid body rotation does not contribute because it does not affect the polarity alignment. Integrating once, we obtain

$$a' = \frac{b_0}{\sin\theta} - \frac{r v_3}{\Gamma} \sin^3\theta, \tag{D28}$$

where b_0 is an integration constant. Finally, we have the general solution

$$a = a_0 + b_0 \log\frac{1-\cos\theta}{1+\cos\theta} + \frac{r v_3}{\Gamma} \cos\theta \left(\frac{2}{3} + \frac{1}{3}\sin^2\theta\right) \tag{D29}$$

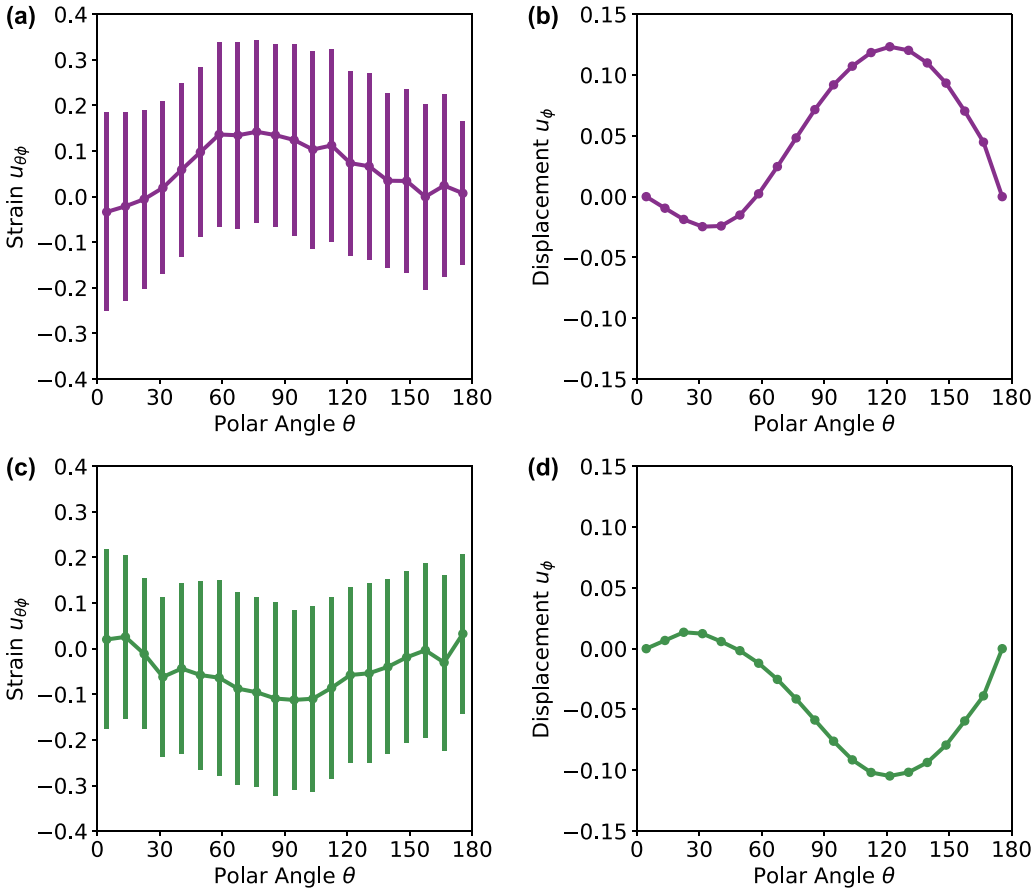

FIG. 20. Inferring displacement from experimental cell shape data. (a),(c) Mean and standard deviation cell strain for (a) sphere 1 ($\beta \approx 45^\circ$) and (c) sphere 2 ($\beta \approx 135^\circ$), as shown in Fig. 5. (b),(d) Inferred displacement u_ϕ against polar angle θ for (b) sphere 1 ($\beta \approx 45^\circ$) and (d) sphere 2 ($\beta \approx 135^\circ$).

with a second integration constant a_0. We note that for $b_0 \neq 0$, the angle diverges towards the poles. We exclude this solution and set $b_0 = 0$. Finally, we define $a_1 = (2rv_3)/(3\Gamma)$ as the corotational magnitude which is equal to the angle change from the equator to the poles due to corotational effects. Thus, our final steady-state polarity angle is given by

$$a = a_0 + a_1 \cos\theta\left(1 + \tfrac{1}{2}\sin^2\theta\right). \tag{D30}$$

For $a_0 \neq 0$, the polarity field is a chiral helix. In this case, the two topological defects at $\theta = 0$ and $\theta = \pi$ are different, with $\nabla \cdot \mathbf{p}$ having opposite signs. Note that for $a_0 = 0$ the system is not chiral, and defects are symmetric. For rigid body rotation, $a_1 = 0$, and the polarity field becomes invariant under $\mathbf{p}(\vec{r}) \to -\mathbf{p}(\vec{r})$ up to global rotations of the sphere.

5. Cell deformation patterns

Traction forces acting on the organoid sphere, consisting of friction and polarity forces $\xi\mathbf{v} - F\mathbf{p}$, induce in-plane elastic strains. These elastic strains correspond to cell deformations and are determined by the force balance of an elastic shell,

$$G\Delta\mathbf{u} + K\mathbf{u} = \nabla P + \xi\mathbf{v} - F\mathbf{p}, \tag{D31}$$

where G is the shear modulus, Δ is the Laplace-Beltrami operator, P is the pressure determined by the incompressibility constraint, and $K = r^{-2}$ is the Gaussian curvature which arises because we are working on the surface of a sphere. Note that Eq. (D15) follows from the (D31) in the steady state. Namely, the gradient of velocity $\mathbf{v}$ due to cell rearrangements is proportional to the in-plane stress, and therefore also to gradients of $\mathbf{u}$.

Using the steady-state polarity field and the solid body rotation velocity field ($v_1 = 0$), we determine the displacement field $\mathbf{u}$ on the sphere's surface. To obtain a tilt angle β that reflects the cell elongation tilt angle, we determine the tilt angle of the local shear strain field. The sphere rotates like a solid body with angular velocity $\boldsymbol{\Omega} = \Omega\mathbf{e}_z$ determined by torque balance between frictional forces and the polarity forces,

$$0 = \int \mathbf{x} \times (\xi\mathbf{v} - F\mathbf{p})dS. \tag{D32}$$

To effectively solve these equations on a sphere, we decompose the polarity, displacement, and velocity fields into vector spherical harmonics as

$$\mathbf{p} = \sum_{l,m} p^{(1)}_{lm}\boldsymbol{\Psi}_{lm} + p^{(2)}_{lm}\boldsymbol{\Phi}_{lm}, \tag{D33}$$

$$\mathbf{u} = \sum_{l,m} u^{(1)}_{lm}\boldsymbol{\Psi}_{lm} + u^{(2)}_{lm}\boldsymbol{\Phi}_{lm}, \tag{D34}$$

$$\mathbf{v} = \sum_{l,m} v^{(1)}_{lm}\boldsymbol{\Psi}_{lm} + v^{(2)}_{lm}\boldsymbol{\Phi}_{lm}, \tag{D35}$$

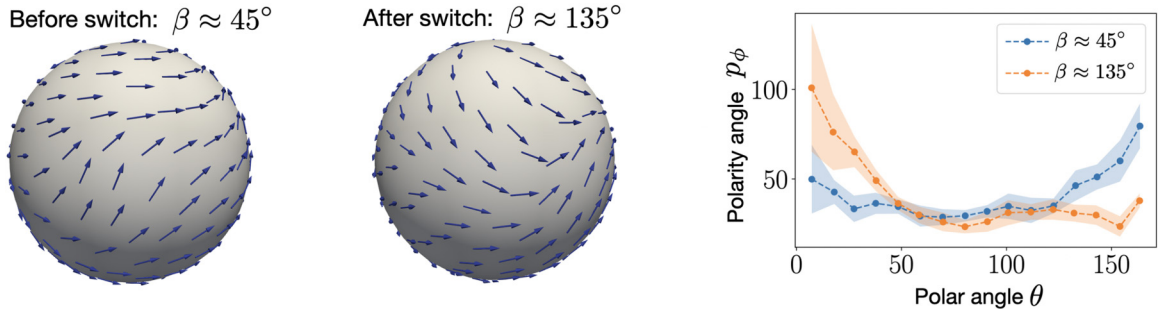

FIG. 21. Polarity pattern in an active vertex model with a switch in the dominant orientation angle. We analyzed the polarity pattern in vertex model simulations with noise in the polarity dynamics. We find that, in contrast to simulations without noise, the peak in the distribution of the cell orientation angle exhibits a switch between $\beta \approx 45°$ and $\beta \approx 135°$. We see a polarity pattern with two topological defects located on the poles. However, the nature and positioning of these topological defects seem to change between the time windows with $\beta \approx 45°$ and $\beta \approx 135°$. This is in good agreement with the predictions from our continuum model (see Fig. 5), although we see that the polarity pattern in the vertex model is not entirely axisymmetric. To quantify the polarity pattern, we compute the angle between the polarity field and the azimuthal direction of rotation $p_\phi = \cos^{-1}(\boldsymbol{p} \cdot \hat{\phi})$ as a function of polar angle θ. The simulations in this figure have parameters $N = 200$, $\overline{\gamma} = 5$, $k = 10$, $\overline{F} = 0.8$, and $\overline{\mathcal{D}} = 0.2$.

and the pressure field into scalar spherical harmonics

$$P = \sum_{l,m} P_{lm} Y_{lm}. \tag{D36}$$

Note that since we are considering axisymmetric solutions, coefficients with $m \neq 0$ vanish.

To determine the rotation rate, we consider the friction contribution to the overall torque,

$$\xi \int \mathbf{x} \times \mathbf{v} dS = \xi \int \mathbf{x} \times (\boldsymbol{\omega} \times \mathbf{x}) dS = \frac{8\pi}{3} \xi \omega r^4 \mathbf{e}_z. \tag{D37}$$

Next we calculate the contribution from cell polarity force, using $\mathbf{x} \times \boldsymbol{\Psi}_{lm} = r \boldsymbol{\Phi}_{lm}$ and $\mathbf{x} \times \boldsymbol{\Phi}_{lm} = -r \boldsymbol{\Psi}_{lm}$. Note that terms involving $\boldsymbol{\Psi}_{lm}$ do not contribute to torque. Next we calculate

$$\int \mathbf{x} \times \boldsymbol{\Phi}_{l0} dS = -2 \int r \sin\theta \frac{\partial Y_{l0}}{\partial \theta} dS \mathbf{e}_z \tag{D38}$$

using the substitution $z = \cos\theta$ and the definition of $Y_{l0} = \sqrt{\frac{2l+1}{4\pi}} P_l(\cos\theta)$, where $P_l(x)$ are the Legendre polynomials, and the integral becomes

$$\int \mathbf{x} \times \boldsymbol{\Phi}_{l0} dS = 2\pi r^3 \int_{-1}^{1} (1 - x^2) P_l'(x) dx. \tag{D39}$$

With the identities $(1 - x^2) P_l'(x) = l P_{l-1}(x) - l x P_l(x)$, the orthogonality of the Legendre polynomials, and $\int_{-1}^{1} P_l(x) P_k(x) dx = \frac{2}{2l+1} \delta_{kl}$, we finally obtain

$$\int \mathbf{x} \times \boldsymbol{\Phi}_{l0} dS = \frac{8\pi}{3} r^3 \mathbf{e}_z \delta_{l,0}. \tag{D40}$$

Therefore, torque balance implies the rotation rate $\omega = (F p_{1,0}^{(2)})/(\xi r)$, and the velocity $\mathbf{v} = (F/\xi) p_{1,0}^{(2)} \boldsymbol{\Phi}_{1,0}$.

Using the incompressibility condition, $\nabla \cdot \mathbf{u} = \mathbf{0}$, and force balance, we find that the pressure satisfies

$$\nabla^2 P = \nabla \cdot (\xi \mathbf{v} - F \mathbf{p}). \tag{D41}$$

This implies that

$$P_{lm} = -rF p_{lm}^{(1)} + c, \tag{D42}$$

where c is a constant. We find the displacement field spherical harmonics $u_{lm}^{(1)} = 0$, because of the incompressibility constraint.

The displacements modes $u_{lm}^{(2)}$ can be obtained from

$$\frac{1}{r^2}[1 - l(l+1)] u_{lm}^{(2)} = \xi v_{lm}^{(2)} - F p_{lm}^{(2)}, \tag{D43}$$

where we have used $\nabla^2 \Phi_{lm} = -\frac{1}{r^2} l(l+1) \phi_{lm}$. We then find

$$u_{lm}^{(2)} = \begin{cases} \frac{Fr^2}{G(l^2+l-1)} p_{lm}^{(2)} & \text{if } l \neq 1 \text{ and } m = 0, \\ 0 & \text{otherwise.} \end{cases} \tag{D44}$$

We use this displacement field to estimate corresponding patterns of cell elongation.

For solid body rotation and $a = a_0$, the resulting cell elongation patterns are mirror symmetric, resulting in vanishing order parameter $|\langle \Delta\beta \rangle|$. If we allow for cell rearrangements that contribute to the perturbation $v_1 \sin 3\theta$ in the velocity field, the symmetry is broken and the order parameter is nonvanishing, indicating chirality of the cell elongation pattern.

6. Estimation of cell elongation orientation angles

We quantify the resulting cell elongation orientation patterns using the elastic displacement field. Starting from small circles, with area $4\pi r^2/200$, at different locations on the sphere we deform these circles by applying the displacement field $\mathbf{u}$: $\mathbf{X}_i = \mathbf{x}_i + \mathbf{u}(\mathbf{x}_i)$, where $\mathbf{x}_i$ are uniformly sampled points on the initial circle, and $\mathbf{X}_i$ are their displaced positions. Circle size is chosen to represent the typical size of cells in experiments and in vertex model simulations. This defines a set of points $\mathbf{x}_i$ that represent a circle. Finally, we quantify the anisotropy of the deformed circles by fitting ellipses. The long ellipse axis defines the tilt angle β of elongation for each circle. To obtain a distribution of tilt angles on the sphere, we place the circle center at latitudes between $\theta = 0$ and $\theta = \pi$, using 1000 points. Additionally, when taking a histogram, each angle θ contributes a weight $\sin\theta$, which is proportional to the number of cells at this latitude.

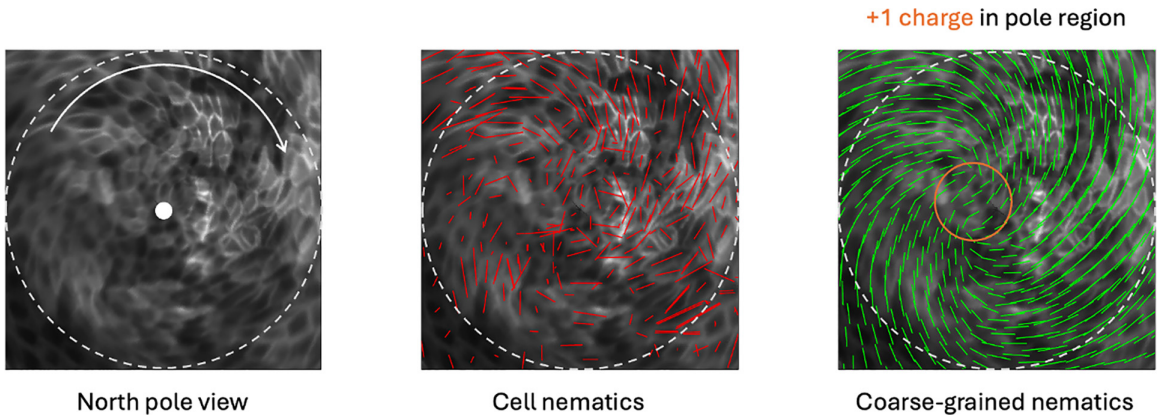

FIG. 22. Cellular packing in the polar region of a rotating sphere. View onto the north pole of a rotating sphere labeled by Myh-14-GFP (left panel). The pole is indicated by the white circle, the equator by the dashed line, and the sense of rotation is indicated by an arrow. The cell elongation nematics are indicated by red bars (center panel). Coarse-grained representation of cell elongation nematics reveals a +1 topological defect charge near the pole (right panel). We analyzed the cell shape nematicity near the pole. The first panel shows the polar projection of the sphere with the rotation direction as indicated. The middle panel shows the nematicity of cells that we calculate directly from cell segmentation. (Note that nematicity for cells that are not segmented properly has been omitted.) Even though the field is rather noisy, by coarse-graining the nematicity field (right panel), we can clearly see a +1 topological defect near the pole, with cell slants near the equator, consistent with results from our continuum model.

APPENDIX E: INFERRING TRACTION FORCE FROM CELL SHAPE

We infer the azimuthal traction force by analyzing cell shapes as the tissue rotates, assuming that the surface of the organoid behaves like the elastic shell described above, implying that a cell's rest configuration is isotropic and it deforms under traction stress. For a cell with aspect ratio a and tilt angle β, we write the strain tensor as

$$\epsilon(\beta) = R(\beta)\epsilon(0)R(\beta)^{-1}, \tag{E1}$$

where $R(\beta)$ is the 2D rotation matrix by angle β, and

$$\epsilon(0) = \begin{pmatrix} \sqrt{a} & 0 \\ 0 & 1/\sqrt{a} \end{pmatrix} \tag{E2}$$

is the strain tensor when aligned with the azimuth. The strain tensor reads

$$\epsilon(\beta) = \begin{pmatrix} \sqrt{a}\sin^2\beta + 1/\sqrt{a}\cos^2\beta - 1 & (\sqrt{a} - 1/\sqrt{a})\sin\beta\cos\beta \\ (\sqrt{a} - 1/\sqrt{a})\sin\beta\cos\beta & \sqrt{a}\cos^2\beta + 1/\sqrt{a}\sin^2\beta - 1 \end{pmatrix}, \tag{E3}$$

where the first coordinates represent the θ components and the second represent the ϕ components.

Next, for each experiment we obtain an average strain tensor ϵ for each angle θ; see Figs. 16(a) and 16(c). The ϕ component $u_\phi(\theta)$ of the displacement field can be obtained using

$$\epsilon_{\theta\phi} = \frac{1}{r}\left(\frac{\partial u_\phi}{\partial\theta} - \cot\theta u_\phi\right) \tag{E4}$$

and integrating, which results in

$$u_\phi = r\sin\theta\int_0^\theta \frac{\epsilon_{\theta\phi}}{\sin\theta'}d\theta'. \tag{E5}$$

Examples of the displacement field are shown in Figs. 20(b) and 20(d). Through force balance in the ϕ direction, we obtain the ϕ component of the traction force,

$$t_\phi = Fp_\phi - \xi v_\phi = \frac{1}{r}G\left(\frac{\partial^2 u_\phi}{\partial\theta^2} + \cot\theta\frac{\partial u_\phi}{\partial\theta} - \frac{1}{\sin^2\theta}u_\phi\right). \tag{E6}$$

This is performed numerically, and results are shown in Figs. 5(j) and 5(k) in the main text.

APPENDIX F: STATISTICS FOR THE EXPERIMENTAL REPLICATES

In Table I, we present the statistics for the experimental replicates.

APPENDIX G: ADDITIONAL FIGURES

Figures 6–22 contain additional information documenting the methods, showing more replicates or supporting the explanations.

APPENDIX H: VIDEOS

The Supplemental Material (SM) [32] contains several videos, the descriptions of which are as follows:

Video 1: Maximum intensity projection of a sphere showing persistent rotation [Fig. 1(f),(i)]. Fluorescence intensity

corresponds to membrane dye ROSAmTmG. Time stamp, hh:mm.

Video 2: Maximum intensity projection of a sphere showing no rotation [Fig. 1(f),(ii)]. Fluorescence intensity corresponds to myosin. Time stamp, hh:mm.

Video 3: Maximum intensity projection of a sphere showing rotation arrest [Fig. 1(g),(i)]. Fluorescence intensity corresponds to myosin. Time stamp, hh:mm.

Video 4: Maximum intensity projection of a sphere showing rotation axis drift [Fig. 1(g),(ii)]. Fluorescence intensity corresponds to membrane dye ROSAmTmG. Time stamp, hh:mm.

Video 5: Particle imaging velocimetry (PIV) performed on three different projections: (i) Mercator projection (top); (ii) "north" pole projection (bottom left); and (iii) "south" pole projection (bottom right). See Appendix B 2 for the equations defining the mapping. Dotted white line corresponds to $\theta = 90^\circ$ (i.e., the "equator"). The projection is done with respect to laboratory frame.

Video 6: Simulation of a sphere in the solid rotation regime. A rotating sphere with aligned cell polarities. In this case, the correlation length of polarities spans the whole system size.

Video 7: Simulation of a sphere near the yielding transition. Due to an interplay between traction force and the polarity alignment mechanisms, patches of cells with aligned polarities form, but their correlation length is less than the system size. Hence, in this case, the rotation axis drifts as patches of aligned polarity cells form and break apart.

Video 8: Simulation of a sphere in the flowing regime. In this case, cell polarity-directed traction forces are uncorrelated. Therefore, randomly oriented traction forces lead to continuous flow of cell rearrangements.

[1] A. Shellard and R. Mayor, Rules of collective migration: From the wildebeest to the neural crest, Philos. Trans. R. Soc. B **375**, 20190387 (2020).

[2] J. Muñoz-Dorado, F. J. Marcos-Torres, E. García-Bravo, A. Moraleda-Muñoz, and J. Pérez, Myxobacteria: Moving, killing, feeding, and surviving together, Front. Microbiol. **7**, 781 (2016).

[3] K. Copenhagen, R. Alert, N. S. Wingreen, and J. W. Shaevitz, Topological defects promote layer formation in myxococcus xanthus colonies, Nat. Phys. **17**, 211 (2021).

[4] J. Stock and A. Pauli, Self-organized cell migration across scales–from single cell movement to tissue formation, Development **148**, dev191767 (2021).

[5] A. Brugués, E. Anon, V. Conte, J. H. Veldhuis, M. Gupta, J. Colombelli, J. J. Muñoz, G. W. Brodland, B. Ladoux, and X. Trepat, Forces driving epithelial wound healing, Nat. Phys. **10**, 683 (2014).

[6] T. B. Saw, A. Doostmohammadi, V. Nier, L. Kocgozlu, S. Thampi, Y. Toyama, P. Marcq, C. T. Lim, J. M. Yeomans, and B. Ladoux, Topological defects in epithelia govern cell death and extrusion, Nature (London) **544**, 212 (2017).

[7] K. Kawaguchi, R. Kageyama, and M. Sano, Topological defects control collective dynamics in neural progenitor cell cultures, Nature (London) **545**, 327 (2017).

[8] A. Livshits, L. Shani-Zerbib, Y. Maroudas-Sacks, E. Braun, and K. Keren, Structural inheritance of the actin cytoskeletal organization determines the body axis in regenerating hydra, Cell Rep. **18**, 1410 (2017).

[9] L. A. Hoffmann, L. N. Carenza, J. Eckert, and L. Giomi, Theory of defect-mediated morphogenesis, Sci. Adv. **8**, eabk2712 (2022).

[10] A. Mongera, P. Rowghanian, H. J. Gustafson, E. Shelton, D. A. Kealhofer, E. K. Carn, F. Serwane, A. A. Lucio, J. Giammona, and O. Campàs, A fluid-to-solid jamming transition underlies vertebrate body axis elongation, Nature (London) **561**, 401 (2018).

[11] M. Saadaoui, D. Rocancourt, J. Roussel, F. Corson, and J. Gros, A tensile ring drives tissue flows to shape the gastrulating amniote embryo, Science **367**, 453 (2020).

[12] F. C. Keber, E. Loiseau, T. Sanchez, S. J. DeCamp, L. Giomi, M. J. Bowick, M. C. Marchetti, Z. Dogic, and A. R. Bausch, Topology and dynamics of active nematic vesicles, Science **345**, 1135 (2014).

[13] P. W. Ellis, D. J. Pearce, Y.-W. Chang, G. Goldsztein, L. Giomi, and A. Fernandez-Nieves, Curvature-induced defect unbinding and dynamics in active nematic toroids, Nat. Phys. **14**, 85 (2018).

[14] S. Shankar, M. J. Bowick, and M. C. Marchetti, Topological sound and flocking on curved surfaces, Phys. Rev. X **7**, 031039 (2017).

[15] K. Doxzen, S. R. K. Vedula, M. C. Leong, H. Hirata, N. S. Gov, A. J. Kabla, B. Ladoux, and C. T. Lim, Guidance of collective cell migration by substrate geometry, Integr. Biol. **5**, 1026 (2013).

[16] Z. Hachem, C. Hadrian, L. Aldbaisi, M. Alkaabi, L. Q. Wan, and J. Fan, Asymmetrical positioning of cell organelles reflects the cell chirality of mouse myoblast cells, APL Bioeng. **8**, 016119 (2023).

[17] P. J. Albert and U. S. Schwarz, Dynamics of cell ensembles on adhesive micropatterns: Bridging the gap between single cell spreading and collective cell migration, PLoS Comput. Biol. **12**, e1004863 (2016).

[18] C. Fang, J. Yao, Y. Zhang, and Y. Lin, Active chemo-mechanical feedbacks dictate the collective migration of cells on patterned surfaces, Biophys. J. **121**, 1266 (2022).

[19] E. Hirata, T. Ichikawa, S.-I. Horike, and E. Kiyokawa, Active k-ras induces the coherent rotation of epithelial cells: A model for collective cell invasion in vitro, Cancer Sci. **109**, 4045 (2018).

[20] A. S. Chin, K. E. Worley, P. Ray, G. Kaur, J. Fan, and L. Q. Wan, Epithelial cell chirality revealed by three-dimensional spontaneous rotation, Proc. Natl. Acad. Sci. (USA) **115**, 12188 (2018).

[21] L. Lu, T. Guyomar, Q. Vagne, R. Berthoz, A. Torres-Sánchez, M. Lieb, C. Martin-Lemaitre, K. Van Unen, A. Honigmann, O. Pertz, D. Riveline, and G. Salbreux, Polarity-driven three-dimensional spontaneous rotation of a cell doublet, Nat. Phys. **20**, 1194 (2024).

[22] F. Ascione, S. Caserta, S. Esposito, V. R. Villella, L. Maiuri, M. R. Nejad, A. Doostmohammadi, J. M. Yeomans, and S. Guido, Collective rotational motion of freely expanding T84 epithelial cell colonies, J. R. Soc. Interface **20**, 20220719 (2023).

[23] T. Brandstätter, D. B. Brückner, Y. L. Han, R. Alert, M. Guo, and C. P. Broedersz, Curvature induces active velocity waves in rotating spherical tissues, Nat. Commun. **14**, 1643 (2023).

[24] K. Barlan, M. Cetera, and S. Horne-Badovinac, Fat2 and lar define a basally localized planar signaling system controlling collective cell migration, Develop. Cell **40**, 467 (2017).

[25] W. Xi, S. Sonam, T. Beng Saw, B. Ladoux, and C. Teck Lim, Emergent patterns of collective cell migration under tubular confinement, Nat. Commun. **8**, 1517 (2017).

[26] A. Glentis, C. Blanch-Mercader, L. Balasubramaniam, T. B. Saw, J. d'Alessandro, S. Janel, A. Douanier, B. Delaval, F. Lafont, C. T. Lim *et al.*, The emergence of spontaneous coordinated epithelial rotation on cylindrical curved surfaces, Sci. Adv. **8**, eabn5406 (2022).

[27] K. Tanner, H. Mori, R. Mroue, A. Bruni-Cardoso, and M. J. Bissell, Coherent angular motion in the establishment of multicellular architecture of glandular tissues, Proc. Natl. Acad. Sci. (USA) **109**, 1973 (2012).

[28] H. Wang, S. Lacoche, L. Huang, B. Xue, and S. K. Muthuswamy, Rotational motion during three-dimensional morphogenesis of mammary epithelial acini relates to laminin matrix assembly, Proc. Natl. Acad. Sci. (USA) **110**, 163 (2013).

[29] P. A. Fernández, B. Buchmann, A. Goychuk, L. K. Engelbrecht, M. K. Raich, C. H. Scheel, E. Frey, and A. R. Bausch, Surface-tension-induced budding drives alveologenesis in human mammary gland organoids, Nat. Phys. **17**, 1130 (2021).

[30] L. Hof, T. Moreth, M. Koch, T. Liebisch, M. Kurtz, J. Tarnick, S. M. Lissek, M. Verstegen, L. J. van der Laan, M. Huch *et al.*, Long-term live imaging and multiscale analysis identify heterogeneity and core principles of epithelial organoid morphogenesis, BMC Biol. **19**, 37 (2021).

[31] C. Greggio, F. De Franceschi, M. Figueiredo-Larsen, S. Gobaa, A. Ranga, H. Semb, M. Lutolf, and A. Grapin-Botton, Artificial three-dimensional niches deconstruct pancreas development in vitro, Development **140**, 4452 (2013).

[32] See Supplemental Material at http://link.aps.org/supplemental/10.1103/PRXLife.2.033006 for several videos.

[33] M. Borries, Y. F. Barooji, S. Yennek, A. Grapin-Botton, K. Berg-Sørensen, and L. B. Oddershede, Quantification of viscoelastic properties of a matrigel for organoid development as a function of polymer concentration, Front. Phys. **8**, 579168 (2020).

[34] R. Farhadifar, J.-C. Röper, B. Aigouy, S. Eaton, and F. Jülicher, The influence of cell mechanics, cell-cell interactions, and proliferation on epithelial packing, Curr. Biol. **17**, 2095 (2007).

[35] D. Bi, X. Yang, M. C. Marchetti, and M. L. Manning, Motility-driven glass and jamming transitions in biological tissues, Phys. Rev. X **6**, 021011 (2016).

[36] M. Popović, V. Druelle, N. A. Dye, F. Jülicher, and M. Wyart, Inferring the flow properties of epithelial tissues from their geometry, New J. Phys. **23**, 033004 (2021).

[37] H. Honda, H. Yamanaka, and M. Dan-Sohkawa, A computer simulation of geometrical configurations during cell division, J. Theor. Biol. **106**, 423 (1984).

[38] A. Amiri, C. Duclut, F. Jülicher, and M. Popović, Random traction yielding transition in epithelial tissues, Phys. Rev. Lett. **131**, 188401 (2023).

[39] N. A. Dye, M. Popović, K. V. Iyer, J. F. Fuhrmann, R. Piscitello-Gómez, S. Eaton, and F. Jülicher, Self-organized patterning of cell morphology via mechanosensitive feedback, Elife **10**, e57964 (2021).

[40] K. Shinohara and H. Hamada, Cilia in left–right symmetry breaking, Cold Spring Harb. Perspect. Biol. **9**, a028282 (2017).

[41] K. Taniguchi, R. Maeda, T. Ando, T. Okumura, N. Nakazawa, R. Hatori, M. Nakamura, S. Hozumi, H. Fujiwara, and K. Matsuno, Chirality in planar cell shape contributes to left-right asymmetric epithelial morphogenesis, Science **333**, 339 (2011).

[42] J. Hadidjojo and D. K. Lubensky, Spontaneous chiral symmetry breaking in planar polarized epithelia, arXiv:1708.08560 (2017).

[43] Q. Yang, S.-L. Xue, C. J. Chan, M. Rempfler, D. Vischi, F. Maurer-Gutierrez, T. Hiiragi, E. Hannezo, and P. Liberali, Cell fate coordinates mechano-osmotic forces in intestinal crypt formation, Nat. Cell Biol. **23**, 733 (2021).

[44] I. Viktorinová and C. Dahmann, Microtubule polarity predicts direction of egg chamber rotation in drosophila, Curr. Biol. **23**, 1472 (2013).

[45] M. Cetera, G. R. Ramirez-San Juan, P. W. Oakes, L. Lewellyn, M. J. Fairchild, G. Tanentzapf, M. L. Gardel, and S. Horne-Badovinac, Epithelial rotation promotes the global alignment of contractile actin bundles during drosophila egg chamber elongation, Nat. Commun. **5**, 5511 (2014).

[46] E. W. Gehrels, B. Chakrabortty, M.-C. Perrin, M. Merkel, and T. Lecuit, Curvature gradient drives polarized tissue flow in the *Drosophila* embryo, Proc. Natl. Acad. Sci. (USA) **120**, e2214205120 (2023).

[47] M. D. Muzumdar, B. Tasic, K. Miyamichi, L. Li, and L. Luo, A global double-fluorescent cre reporter mouse, genesis **45**, 593 (2007).

[48] S. Berg, D. Kutra, T. Kroeger, C. N. Straehle, B. X. Kausler, C. Haubold, M. Schiegg, J. Ales, T. Beier, M. Rudy *et al.*, Ilastik: Interactive machine learning for (bio) image analysis, Nat. Methods **16**, 1226 (2019).

[49] W. Thielicke and R. Sonntag, Particle image velocimetry for matlab: Accuracy and enhanced algorithms in pivlab, J. Open Res. Software **9**, 12 (2021).

[50] B. Aigouy, C. Cortes, S. Liu, and B. Prud'Homme, Epyseg: A coding-free solution for automated segmentation of epithelia using deep learning, Development **147**, dev.194589 (2020).